Universitetet
i Stavanger

FACULTY OF SCIENCE AND TECHNOLOGY

MASTER'S THESIS

Study programme: Mechanical and Structural Engineering and Materials Science Specialisation: Offshore Structures	Spring semester, 2017 Open
Author: Mathias O. M. Haugen	Mathias O.M. Haugen (signature of author)
Faculty supervisor: Professor Muk Chen Ong External supervisor: Dr. Guomin Ji	
Title of master's thesis: Finite Element Models for Integrity Assessment of Flexible Riser with Damaged Tensile Wires	
Credits: 30	
Keywords: • Flexible riser • Damaged tensile wires • FEM • Abaqus	Number of pages: 80 + supplemental: ..... Stavanger, 1/7-2017 date/2017

Abstract

Many of the flexible risers in service do not meet their documented service life. A common failure mode is the rupture of the abrasive external layer which, in itself, is not critical, but seawater ingress may corrode tensile wires over time and, in worst case, cause breakage. Damaged tensile armour could significantly reduce the load capacity of the riser. Integrity assessment of flexible riser with damaged tensile armour based on stress concentration factors (SCF) could predict the remaining fatigue life of the structure. SCF could be based on experimental tests, but they are expensive. Finite element analyses can be used instead at a much lower cost.

In this thesis, three finite element models are created in Abaqus to replicate a 2.5 inch flexible riser. In the first model, the tensile wires are represented by beam elements and the other layers by shell elements. In the second and third model, the tensile wires are represented by solid elements and the other layers are represented by shell and solid elements, respectively. However, only the two last models are used in the analyses. To reduce simulation time, the carcass and pressure armour are modelled in a simplified manner with equivalent material properties.

A convergence study is performed to find the minimum element size needed to yield good results. The equivalent material properties used in the simplified layers are evaluated by comparing the hoop stress to analytical values which are in good agreement. Two load cases are considered in the stress analyses, where one is tension and the other is bending. The models are verified by comparing the axial stiffness to the physical one and axial wire stress due to bending to analytical values found in the literature. Both are in good agreement.

A simulation is performed for the second model with two ruptured wires in the outer tensile layer. A tress concentration factor is established based on the current stress results for the mean axial wire stress. The stress concentration factor is compared to results in the literature and show good agreement.

Preface

This report is the result of my master thesis work in offshore structural engineering at the Department of Mechanical and Structural Engineering and Materials Science, University of Stavanger. My thesis work has been a collaboration with Sintef Ocean on the subject of finite element modelling of flexible riser with damaged tensile wires. My knowledge on the matter of flexible risers was limited at the start of the project, and Abaqus, the finite element software used in this work was completely new to me. A big part of this work has been to understand and familiarize both flexible risers and the numerical software.

First of all I would like to thank my department supervisor Professor Muk Chen Ong for giving me the opportunity to work on such a complex and interesting topic and for the help and support during consultations regarding my general thesis work.

Secondly I would like to thank my external supervisor Dr. Guomin Ji. Our discussions on the subject of flexible risers and finite element modelling has been truly encouraging and educational. His instructions and knowledge has provided me with tools necessary to do this work.

Thirdly, I would like to thank Theodor Ivesdal and Ove Kjetil Mikkelsen for useful tips and help regarding OS, servers and software.

Table of contents

1 Introduction

1.1 Background

Flexible risers have been used increasingly in the oil and gas industry for almost 40 years to transfer fluids, mainly, between subsea installations and floating structures. Due to its dynamic properties, the flexible riser is well suited for shallow water and large floater motions. Buoyancy elements can be added in different configurations to uncouple the riser bottom section from the floater motions. By allowing different levels of flexibility, the riser is suited for different field conditions [1].

Although the flexible riser plays an important role in the operation of many oil and gas fields, there are some issues related to this type of riser. Updated Norwegian statistics for 2010-13 show at least 1.5% probability of failure per riser per operational year. Historically, more than 25% of risers on the Norwegian continental shelf have been replaced and only few risers have met their originally documented service life [2]. This illustrates that the industry is facing some issues related to the reliability of flexible risers. Furthermore, the need to repair and replace damaged risers is a source of increased operational cost in terms of replacement expenses and downtime in production during the replacement.

A flexible riser is a multi-layered structure with many potential failure modes. Failure may be triggered during the transportation phase, installation phase, or operational phase of the riser lifecycle [3]. Various data on incidents of flexible riser failure have been gathered worldwide and sorted by failure type. The results showed that the most common failure mode, making up 35% of all incidents, was external sheath damage [4]. Full penetration of the external sheath will allow ingress of seawater into the pipe annulus, thus leaving the carbon steel tension wires exposed to a highly corrosive environment. Over time corrosion pits may develop, which can reduce the fatigue strength of the tension wires significantly [5]. In worst case, this could result in rupture of tensile armour wires, which is one of the most severe failure modes, as it threatens the structural capacity of the riser and may lead to the failure of the whole structure. Ruptured wires could reduce radial support of the layers within. Without sufficient support, the internal plastic sheath could experience local failure causing leakage, and potentially causing total pipe rupture. Additionally, broken wires creating unbalanced torsion distribution over tensile armour cross section could lead to pipe twisting [6].

To reduce operational cost, and ensure safe and reliable operation, it is necessary to assess the structural integrity of flexible risers with damaged tensile wires. Stresses in a rigid riser can be calculated by simple formulas during global analysis, but for flexible risers, on the other hand, the evaluation of stresses in their internal layers is not that simple due to their multi-layered structure and complex response to mechanical loads, especially when friction between the internal layers are considered [7]. Furthermore, for a flexible riser with damaged tension wires, the need to represent each wire individually makes the analysis even more difficult. Existing analytical models for predicting the axisymmetric loading in these pipes (i.e. [8] and [9]) are generally not applicable as they assume the same stress state in all tensile wires and are represented in total geometric properties, which is invalid in the case of ruptured tensile wires [10].

1.2 Concept and configurations of flexible risers

Flexible pipes are a competitive alternative to rigid steel pipes as the low bending stiffness allows large deflections and cyclic loading, making it capable of handling a rough environment and large floater motions. Other advantages are its uncomplicated installation, potential reuse, and non-usage of heave-compensators or tensioners to connecting to floating production units when used as a riser. The high tolerance for cyclic loading makes the flexible pipe concept suitable for several applications. The main applications for flexible pipes are as follows:

- Flexible riser transporting hydrocarbons from wellhead to a fixed rig or floating production unit.
- Flexible jumper transporting hydrocarbons from buoy to floating production unit or from floating production unit to storage tanker.
- Flexible spool connecting subsea structure to flow lines or other subsea structures.

When used as risers, the flexible pipe can have various configurations to adapt to the physical conditions at the location of operation. The different configurations are created by adding buoyancy elements and tethers at different places of the riser to uncouple the bottom connection from the floater motions. Configurations like steep wave, lazy wave, and free hanging (see **Figure 1-1**), are some of the primary configurations which larger compound riser systems are based on.

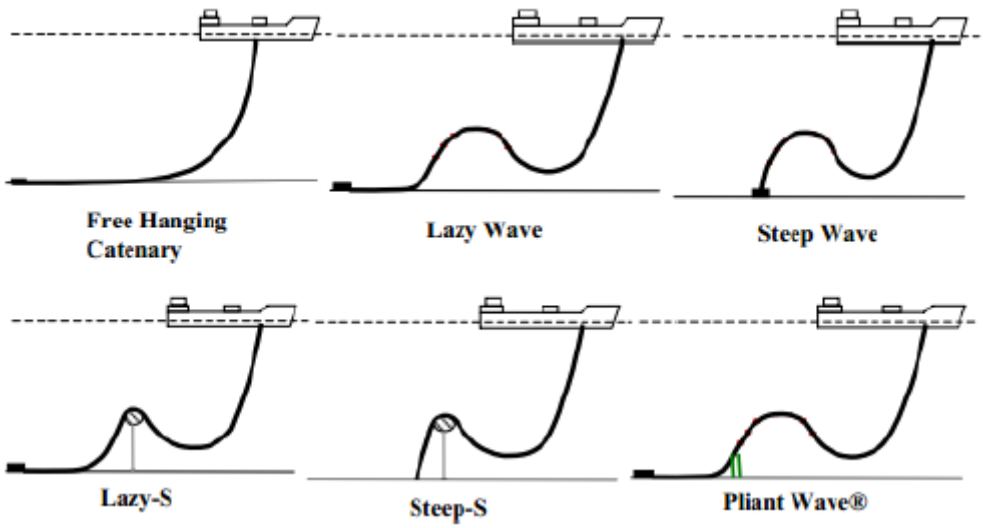

Figure 1-1: Flexible riser configurations.

1.3 Flexible riser cross section

The composition of a flexible riser varies from case to case, as it is a custom-made product designed specifically for the operating conditions of the site where it will be installed. In general, a flexible riser consists of six main layers, namely: carcass, internal plastic sheath, pressure armour, anti-wear tape, tensile armour, and outer plastic sheath (see **Figure 1-2**).

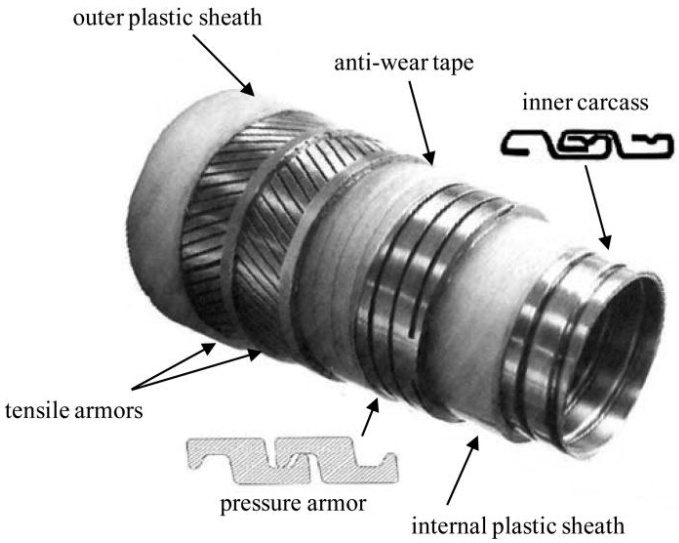

Figure 1-2: Typical flexible riser cross section.

(i)

Inner carcass

The main function of the inner carcass is to prevent the internal plastic layer from collapsing by withstanding the external pressure. As the innermost layer and the only metallic layer in direct contact with the transported fluid, the carcass can be exposed to a highly corrosive environment. Therefore, stainless steel is the most common material in use. In production, a continuous strip of metal feeding onto a mandrel forming a helix with s-shaped profile (see **Figure 1-3**). Every turn interlock with the next, creating an interlocked tube.

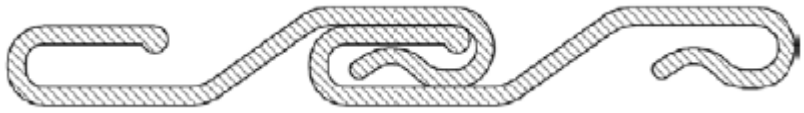

Figure 1-3: Carcass strip profile.

(ii)

Internal plastic sheath

Extruded onto the carcass, this layer, also called liner, serves the purpose of a seal between carcass and the external layers of the riser. The liner is exposed to the bore fluid. Depending on the design conditions like temperature and chemical composition of the fluid, the internal plastic layer can be made of different types of plastics. Sometimes, a sacrificial layer is added inside and/or outside the sealing layer to protect the liner from the metallic layers.

(iii)

Pressure armour

Made of cold rolled carbon steel, the pressure armour serves mainly as a hoop stress barrier by resisting the internal pressure. Pressure armour is an interlocking profile with a helical shape. Lay direction is close to ninety degrees from the longitudinal pipe axis. The profiles are either zeta shaped (**Figure 1-4**), c-clip shaped, or theta shaped (**Figure 1-5**).

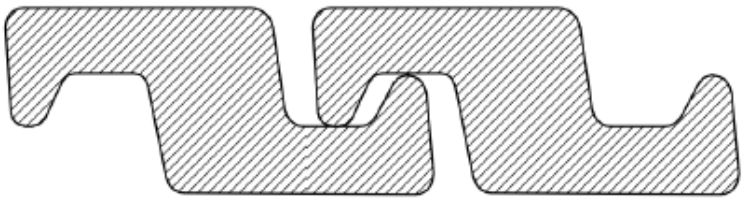

Figure 1-4: Zeta profile pressure armour.

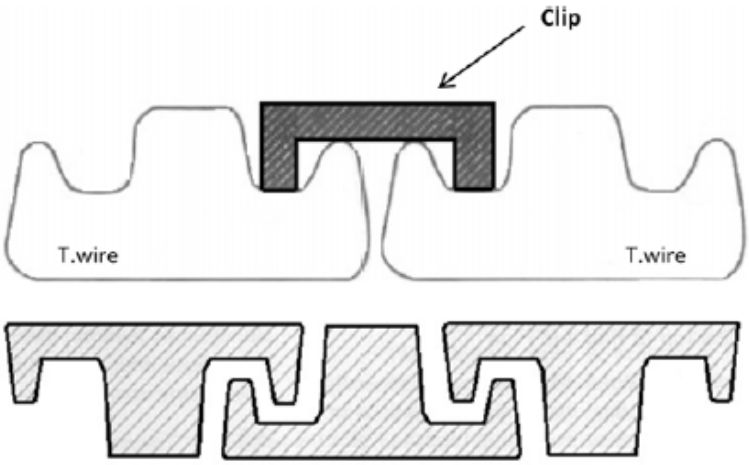

Figure 1-5: Theta profile pressure armour.

(iv)

Anti-wear tape

Adjacent layers of the flexible pipe will slide relative to each other during cyclic bending causing large contact stresses. If two steel layers are in direct contact during this process, there may be wear or fretting fatigue. To avoid this, a layer of plastic anti-wear tape is applied between steel layers. The anti-wear tape is not leak proof.

(v)

Tensile armour

Each tensile armour layer is made up of several carbon steel wires with an almost rectangular cross section laid at an angle usually between 30 and 35 degrees from the pipe longitudinal axis giving it a helical shape. The purpose of the tensile armour is to give the pipe tensile strength to resist axial stress due to internal pressure and external forces. There is usually two or four layers of tensile armour and the lay direction of each layer alternate to avoid torsion during tension loading.

(vi)

Fabric tape

Torsional loading in the opposite direction of the outer tensile armour lay and axial compressive loads are load conditions in which the outer tensile armour is vulnerable. Exposed to these conditions, radial buckling also called bird-caging and lateral buckling may occur. As a result, a layer of fibre-tape (anti-buckling tape) can be applied outside of the outer tensile armour layer to give it radial support.

(vii)

External plastic sheath

An outer plastic sheath envelops the rest of the pipe layers. The main functions of the outermost layer are to protect from abrasive damage, and to seal against seawater avoiding corrosion damage in the steel layers within. Loads on the outer sheath are usually erosion, impact, tear, and, in some cases external and internal pressure.

1.4 Failure modes for flexible pipe

This section is based on API Recommended Practice 17B [4], where failure mode is defined as the manifestation of loss of functionality for a layer in the pipe cross section, and it is the manner by which a failure is observed. Various failure modes (ref. **Table 1-1**) can progress to an ultimate failure, which is defined as failure that leads to loss of functionality. Ultimate failure can be divided into four main categories:

- Loss of containment – full pipe separation
- Loss of containment – leakage
- Blockage or restriction of the flow path caused by failure of a pipe layer (carcass or liner collapse)
- Blockage or restriction of the flow path caused by the bore medium and the bore conditions, or equipment used in pipe or well.

Pipe failure is often the result of several small events of less severity that, over time and in sum, become critical for the pipe structure. One example is a wound in the external plastic sheath allowing ingress of seawater in the pipe annulus which in itself not critical, but with time, tensile wire cross sections may reduce due to corrosion damage which may cause failure

of tensile wires. The progress of pipe failure is often referred to as a failure mechanism and can generally be described as:

1. Initiation of failure and deterioration of the layer
    - Time, event or condition based failure causes
2. Observed failure mode (layer failure)
    - Local failure effect (consequence for the layer itself)
3. Failure of subsequent layers governed by associated failure cause

4. The ultimate loss of pipe functionality

In the process of designing a flexible riser, it is important to familiarize and understand the different modes of failure to secure the product`s durability and reliability throughout its lifespan. The list of possible failure modes is a long one. Assuming perfect manufacturing, transport and installation, what is left is the failure modes that may occur during operation. API 17 B provides a list of failure modes and mechanisms that are most likely to occur during operation [11]:

Table 1-1- Failure modes and mechanisms for flexible pipes.

Failure Modes	Potential Failure Mechanisms
Collapse	1. Collapse of carcass and/or pressure armour due to excess tension. 2. Collapse of carcass and/or pressure armours due to excess external pressure. 3. Collapse of internal pressure sheath in smooth bore pipe.
Burst	1. Rupture of pressure armour because of excessive internal pressure. 2. Rupture of tensile armours due to excess internal pressure.
Tensile failure	1. Rupture of tensile armour due to excess tension. 2. Collapse of carcass and/or pressure armour and/or internal pressure sheath due to excess tension. 3. Snagging by fishing trawl board anchor, causing over-bending or tensile failure.
Compressive failure	1. Bird-caging of tensile armour wires. 2. Compression leading to upheaval buckling and excess bending.
Over-bending	1. Collapse of carcass and/or pressure armour or internal pressure sheath. 2. Rupture of internal pressure sheath. 3. Unlocking of interlocked pressure or tensile armour layer. 4. Crack in outer sheath.
Torsional failure	1. Failure of tensile armour wires. 2. Collapse of carcass and/or internal pressure sheath. 3. Bird-caging of tensile armour wires.
Fatigue failure	1. Tensile armour wire fatigue. 2. Pressure armour wire fatigue.
Erosion	1. Erosion of internal carcass.
Corrosion	1. Corrosion of internal carcass. 2. Corrosion of pressure or tensile armour exposed to seawater, if applicable. 3. Corrosion of pressure or tensile armour exposed to diffused product.

1.5 Design criteria for flexible pipe

The structural complexity of flexible pipes and the significant consequences of a potential spill render the importance of thorough work in the design process. Flexible risers are subject to firm regulations and requirements with the aim to achieve long lasting and reliable equipment that can safely transport hydrocarbons under varying load conditions. Three types of analyses are conducted during design of flexible pipes:

- Local cross section analysis to estimate load distribution between the individual layers of the pipe and determine mechanical properties of the cross section.
- Global dynamic response analysis due to environmental loading and installation related loads.
- Fatigue analysis of flexible pipe subject to cyclic loading.

This section will describe the characteristic design requirements corresponding to the different layers of the flexible pipe considered in this project, in accordance to API Specification 17J [12].

(i)

Carcass

The purpose of the carcass layer is to resist external pressure and keep the internal plastic sheath from collapsing. In order to fulfil this purpose, the carcass must be designed with a minimum internal pressure and a maximum external pressure to avoid collapse itself. Designing for external pressure should take into consideration the contact layers from outer layers, hydrostatic pressure and pressure build-up between polymeric layers. Limits for maximum ovality and minimum operational bend radius must also be set to fulfil this purpose. The carcass being in direct contact with the transported fluids is prone to erosion and corrosion. Therefore, the layer must be designed to withstand the erosion and corrosion rates for the specified fluid content over the service life of the pipe. Lastly, the carcass should be designed against buckling, which is evaluated by testing.

(ii)

Internal plastic sheath

The internal plastic sheath is liable to experience creep and strain under operation conditions. The polymeric tubing might creep into the cavasses of the pressure armour due to radial expansion, torsion, pipe bending, axial elongation and compression. This must be taken into account during wall thickness calculations. Furthermore, in addition to contact pressure, this layer will experience aging and absorption of fluids, resulting in change of material properties and performance.

(ii)

Pressure armour

The flexible pipe should be designed for a minimum bend radius that the pipe can obtain without the pressure armour unlocking. After the minimum bend radius is defined, measures can be taken to prevent the bending from exceeding this limiting radius by adding bend stiffeners or bell mounts. Stresses in the pressure armour must not exceed allowable stress to avoid plastic deformation. The design should also account for residual stresses from the manufacturing process and factory acceptance tests. Furthermore, the pressure armour must have sufficient hoop strength and designed against buckling failure, which must be evaluated by testing.

(iii)

Anti-wear

The purpose of the anti-wear layers is to prevent the steel layers or steel and polymeric layers from grinding against each other which effectively shortens the service life of the pipe. The design must take into account wear and aging.

(iv)

Tensile Armour

Stresses in the tensile armour must not exceed allowable stress of the material and the layer must meet the strength requirement. The tensile armour must resist two cases of torsion. The first case is when the torsion acts in the lay direction of the outer armour layer, effectively pressing the outer layer against the inner tensile armour creating tensile forces. The second case is if the torsion acts in the opposite direction, creating gaps between the armour layers. Torsion creating a gap equal to half the thickness of an armour wire is considered as damaging torsion. Compression can cause radial buckling of the armour wires, often referred to as bird caging. Compression causing a gap between the tensile armours and underlying layers equal to half the thickness of the tensile wire is considered as allowable compression. The design should also account for lateral buckling, in addition to corrosion and wear between wires.

(v)

Anti-buckling tape

The purpose of the anti-buckling tape is to prevent radial buckling of the tensile armour. Therefore, they should be designed to meet the required strength throughout the service life of the pipe.

(vi)

External plastic sheath

Similarly to the internal plastic sheath, the external plastic sheath can experience creep and strain. The polymeric tubing might creep into gaps between tensile armour wires under

operational conditions when subjected to external and annulus pressure, axial elongation, pipe bending and compression torque loads. Additionally, changes in material properties and performance due to absorption of fluids into the material matrix, aging and marine growth should be considered in the design process.

(vii)

Service life

In addition to the layer specific design criteria above, criteria concerning fatigue and material degradation must be taken into account during design. Several types of fatigue progressions may take place during service and each of them should be assessed with great care.

1.6 Problem statement

Uncertainty in the remaining fatigue life and failure of flexible risers is still a subject of concern in the oil and gas industry. Although the complex nonlinear behaviour is not fully understood, the development of cross section analysis of flexible risers continue to improve with the aid of finite element software, yielding increasingly advanced models and more accurate integrity assessments. As the finite element models become more advanced, the number of nodes and degrees of freedom (DOF) could increase in orders of magnitude, resulting to substantial computational effort. To reduce time and cost of computation, it is desirable to develop finite element (FE) models which can yield good results with smaller number of nodes and DOF.

1.7 Objectives and scope of thesis

This work is built around 3D Finite Element analyses (FEA) of damaged tensile wires in an unbonded flexible riser using Abaqus CAE. The focus of this study is on the integrity assessment procedure using beam and solid elements to represent the tensile wires, and the aim is to validate the FE models for use in integrity assessment procedures. The analyses will simulate a flexible riser exposed to pure tension and bending loads similar to the study by De Sosa et al. [13]. The analyses' results will be compared to results available in the literature. To accomplish the objectives, the following milestones must be overcome:

- Understand the theory: behaviour of flexible risers under loading and friction between layers
- Understand FEA; structural and continuum elements and contact modelling
- Create the FE models: based on geometry and material properties
- Set up load scenarios for intact and damaged wires for the models and run simulations
- Post process the results
- Calculate stress concentration factors
- Compare results with results in the literature

The present work considers unbonded flexible pipe only. From here on out, the term flexible pipe/riser is used referring to unbonded flexible pipe without specifying this. Furthermore, the integrity assessment is not performed to full extent. The stress concentration factors are calculated, but they are not implemented and used in fatigue analyses.

1.8 Layout of thesis

Chapter 1 is an introduction to both flexible risers and this report. Here, the background of the problem is presented. Furthermore, the geometry and functions of each pipe layer are explained in addition to general applications of flexible pipes. After design criteria and failure modes, the problem statement and objects of the current work are presented.

Chapter 2 considers analytical methods in cross section analyses of flexible risers. Specifically, the behaviour of flexible risers under tensile and bending loads are addressed, in addition to governing stress components and equations for prediction of wire stresses.

Chapter 3 introduces numerical methods used in flexible riser analyses. State of the art in finite element modelling of flexible risers is discussed in this chapter. A brief review of Abaqus and relevant features of the software is also included in this chapter.

Chapter 4 is about equivalent material properties used to simplify the complex geometry of carcass and pressure armour in finite element models. A couple of approaches are presented in addition to criteria for stable orthotropic material and possible evaluation methods for the equivalent properties.

Chapter 5 is the methodology section, which intends to describe how and why the different aspects of modelling are done. Data on the physical riser is presented here in addition to the FE models and elements used. The equivalent properties calculations are shown, as are the loading scenarios and boundary conditions.

In Chapter 6, the calculated equivalent properties are evaluated by comparing the hoop stress of the simplified layers to analytical values. A convergence study is performed to reduce computational effort and lastly the models are validated.

In Chapter 7, analysis results are presented for the models with intact and ruptured tensile wires for tensile loads and combined tensile and bending loads.

Chapter 8 summarizes the main results and gives recommendation for further work.

2 Analytical Methods in Flexible Pipe Analysis

Local cross section analysis is the foundation for design of flexible risers, and is performed to determine the mechanical properties, stress distributions and failure mechanisms which may occur during the transport, installation, and service phase. Although global response analysis and fatigue life analysis are part of the design process, this work will only consider the local cross section analysis.

Over the last decades, there has been multiple publications on analytical local cross section analysis. There are mainly two approaches used. The first one is the classical approach, where the flexible pipe is modelled as one unified and homogeneous structure with cross sectional and material properties equivalent to the sum of contributions from each individual layer. Benefits of the classical approach are effectiveness and ease of computation. The other approach is the multi layered approach, which allows for more detailed and accurate description of the tension, moment and shear in the individual layers, in addition to the interaction between layers of the flexible pipe. The present work will only consider the multi-layered approach as the classical approach is too simplified for use in local stress analyses in the different components of a flexible pipe.

2.1 Flexible pipe response mechanisms

The response of a flexible pipe subject to axisymmetric loads and bending loads is determined by the geometrical and material properties of the cross section. Tension, torsion, internal and external pressure are categorised as axisymmetric loads. To investigate the response of flexible pipes efficiently, it is favourable to differentiate bending loads and axisymmetric loads, and consider the bending and axial loads acting on the tensile wires to be decoupled (see **Figure 2-1**). The structural response of a flexible pipe subject to axisymmetric loads will be linear, assuming that the loading is within the pipe design limits (i.e. displacement due to tension loading as shown in **Figure 2-2a**). On the other hand, structural response due to bending loads are nonlinear. This behaviour is governed by a stick-slip mechanism between tensile wires and adjacent layers, which is determined by the curvature of the pipe. Although the bending response is nonlinear as a whole, it is made up of several approximately linear sections as shown in **Figure 2-2b**.

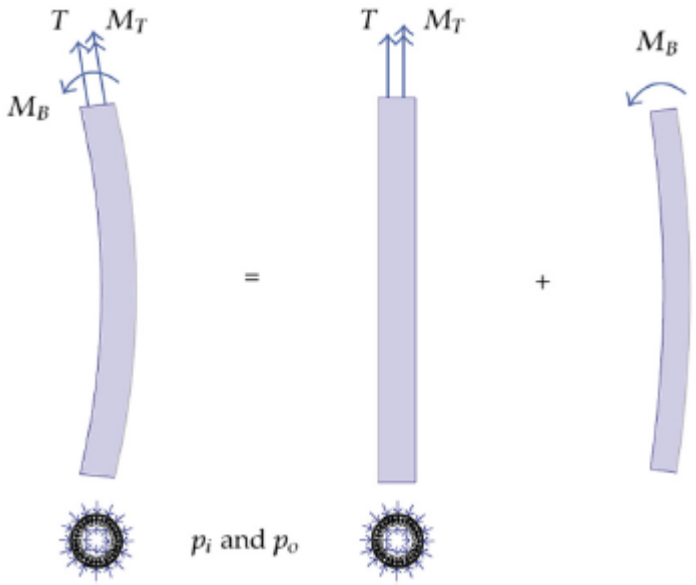

Figure 2-1: Flexible pipe decoupled loads.

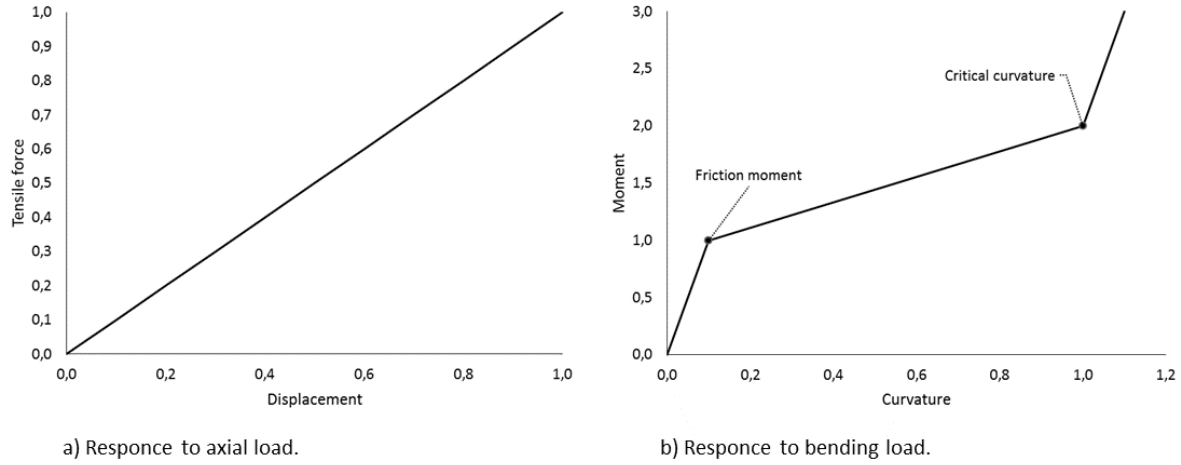

Figure 2-2: Flexible pipe normalized response to loading.

When the bending causes a small pipe curvature, tension will increase within the wires trying to create slip, but the friction between the tensile armour and adjacent layers will keep the wires from sliding along their helical path (stick). Due to Newton's second law, the tensile force and the opposing friction force will maintain a state of equilibrium. Furthermore, the flexible pipe will have approximately the same bending stiffness as a rigid pipe. Increasing the bending and curvature, the tensile force will grow in magnitude and become larger than the static friction force. This point is often referred to as the friction moment, M_f. Now, the layers will start to slip, and the bending stiffness will be reduced significantly. The pipe`s bending stiffness during slip is defined, for the most part, by the sum of contributions from each polymer layer, and additionally, contributions from the individual tensile wires. As the moment and curvature increase further, the slip bending stiffness remains constant until all

gaps between wires are closed and the tendons are once again sticking. At this point, the pipe reaches critical curvature, therefore defining the design limit of the structure. Beyond this point the bending stiffness becomes much larger (see **Figure 2-2b**).

Consider a flexible pipe subject to cyclic bending loading. Starting at zero moment and curvature and loaded to the critical curvature, one half cycle is completed. As the load is reversed from the point of critical curvature, the friction keeps the tendons in the displaced position, preventing them from slipping back the same path. As curvature decrease, the tension and bending moment will reduce linearly and return to zero bending moment at a point of non-zero curvature as shown in **Figure 2-3**. As the cyclic loading continues, the graph take the form of a hysteresis loop.

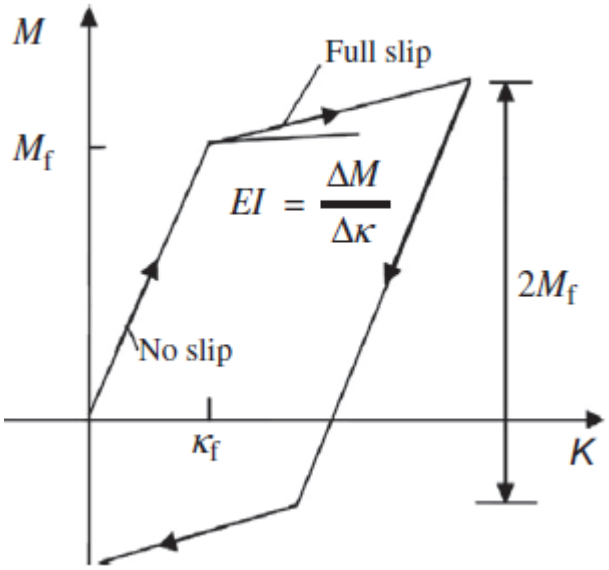

Figure 2-3: Flexible pipe cyclic bending behaviour.

2.2 Stress analysis

Considering a flexible pipe subject to tension and bending, it is clear that the tensile armours govern response. Moreover, wires in the tensile armour are generally assumed to rest stress free in the helix configuration because of plastic straining during manufacturing [4]. Due to linear behaviour during axisymmetric loading, it is not so hard to analytically describe the relationship between response and axisymmetric loading for flexible pipe. This is because the shape of the pipe remain cylindrical during loading and that the loads are symmetric. Bending loads, on the other hand, are not symmetrical. Furthermore, the stick slip mechanism makes describing the relationship between responses and bending loads much more challenging. In the following text, dominant stresses and equations describing load/response relationships are presented. Equations and stresses are in accordance with the wirer coordinates and mechanical quantities shown in **Figure 2-4**. Note that the angular coordinate, Ψ, is measured from the axis normal to the bending direction.

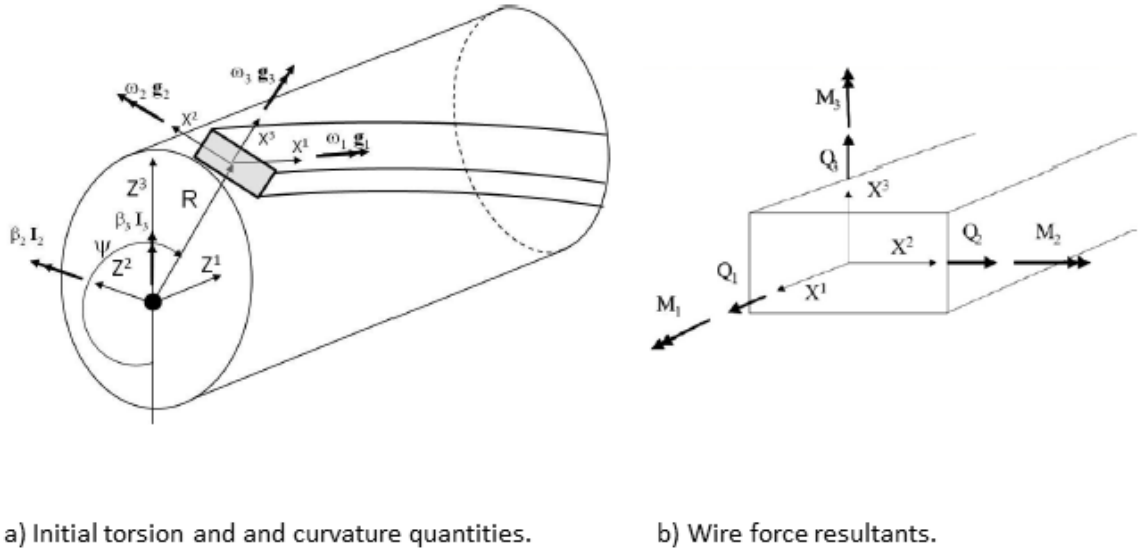

a) Initial torsion and and curvature quantities. b) Wire force resultants.

Figure 2-4: Definition of wire coordinate axes and mechanical quantities.

(i)

Dominant stresses

Flexible pipe consists of concentric layers. All of which have a specific function. To serve their purpose, the individual layers exhibit different cross section, and material properties. To investigate the behaviour in tension and bending, it is necessary to identify the contributing stress components and layers. In a load situation, the metal layers will dominate response. Although, the polymer layers will affect the distribution of load between layers. Considering tensile and bending loads, it is the tensile armour which dominates response. Relevant stresses and their distributions are shown in **Figure 2-5**. $\sigma_{11}^{Q_1}$ is the axial stress due to axial force and friction, and it is uniformly distributed over wire cross section. $\sigma_{11}^{M_2}$ is the bending stress due to bending moment with respect to the weak axis, and it is distributed over wire thickness. $\sigma_{11}^{M_3}$ is the bending stress due bending moment with respect to the strong axis, and it is distributed over wire width. σ_{23} is the torsion stress due to bending, and it is distributed normal to cross section and acting in the directions parallel to cross section edges.

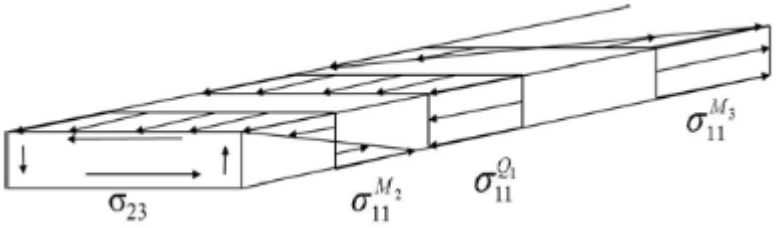

Figure 2-5: Stress components in tensile wires.

(ii)

Tension

Tensile loading is, for the most part, handled by the helical tensile armour layers of the flexible pipe. The contribution of the polymer layers is insignificant, and due to the large lay angle of carcass and pressure armour their resistance is small in comparison to the tensile armour. Including all steel layers and ignoring the polymer layers, axial equilibrium could be expressed as [4]:

$$\sum_{j=1}^{N_a} n_j \sigma_j A_j cos\alpha_j = T_w = T + \pi p_{int} R_{int}^2 - \pi p_{ext} R_{ext}^2 \quad 2.1$$

Where N_a is the number of layers contributing to the axial resistance, α is the lay angle of tensile wires, T_w is the true wall tension, n_j is the number of wires in layer j, σ_j is the axial stress in the layer, A_j is the cross section area of the wire, and T is the effective tension. For a pipe with two layers of tensile armour, assuming equal magnitude of lay angles, but opposite directions, the following equation could be used to predict stresses in the tensile armour:

$$\sigma_t = \frac{T_w}{nA_t cos\alpha} \quad 2.2$$

Where n is the sum of armour wires and A_t is the area of the wire. When the tensile armours are subject to tension loading they will try to compress towards the pipe centre, but the layers within will resist this. The result of this interaction is a contact pressure between the tensile armour and the underlying layers. By assuming the same number of wires for the two layers, the theoretical contact could be estimated by:

$$p_t = \frac{T_w \tan^2 \alpha}{2\pi R^2} \quad 2.3$$

Where R is the mean radius of the tensile armour layers.

(iii)

Bending

Describing the relationship between bending loads and response for flexible pipe in terms of analytical equations is complicated. This is mainly due to the non-linear moment-curvature relation. Especially, calculating stresses in the tensile armour as the tendons are slipping can be challenging. To do so, the following assumptions are applied:

- Constant pipe curvature
- The path which tensile wires move along during slip.

The path can either be a loxodromic curve or a geodesic curve. The loxodromic curve is defined as the initial path of each wire on the underlying cylinder surface. In this case, the wires slip only in their lay direction, and will have curvature with respect to the weak and the strong axis. The geodesic curve on the other hand, is defined as the shortest curve between two sufficiently close points on the underlying cylinder surface. In this case, the wires slip both in the normal and lay direction. Moreover, the wires will have curvature with respect to the weak axis only, but in return, it will be larger than for the loxodromic curve. The geodesic and the loxodromic are extremes. Both can be considered as the outer limits for possible wire paths, where geodesic is the path that the wire would move towards without friction or moderating cross section forces/moments. In the other end of the scale, the loxodromic is the path which the wire would undertake in the case of infinite friction. Of course, in reality, wires will follow a path somewhere in-between the two extremes.

Three of the mechanisms which contribute to axial wire stress during bending are considered here; bending about the weak wire axis (normal curvature), bending about the strong wire axis (bi-normal curvature) and friction between the wire surface and adjacent surfaces. Axial stress due to torsion will also occur, but it is not considered in the present work. Assuming wires undertake the geodesic path, then dynamic stresses due to change in global curvature $\Delta\kappa$ can be expressed in the following manner [14].

For normal curvature:

$$\Delta\sigma_{11}^{M_2} = \frac{3}{2}\cos^2\alpha\,\Delta\kappa t E\cos\psi \tag{2.4}$$

Where t is wire thickness and E is Young`s modulus. For bi-normal curvature:

$$\Delta\sigma_{11}^{M_3} = 0 \tag{2.5}$$

For stress related to friction:

$$\sigma_{11}^{Q_1} = min\left(ER\ \cos^2\alpha\,\Delta\kappa\cos\psi\,, 2\left[\frac{\pi R}{2\sin\alpha\,A}(p_0 + p_i)b(1+e)\mu\cos\psi\right]\right) \tag{2.6}$$

Where μ is the friction coefficient and e is a factor used to calculate the gap between wires (eb = wire gap and b is the wire breadth). A, and E are the wire cross section area and Young's modulus in this order: p_i and p_o are the internal and external pressure, respectively. Assuming wires undertake the loxodromic path, then dynamic stresses due to change in global curvature can be expressed in the following way [14].

For normal curvature:

$$\Delta\sigma_{11}^{M_2} = \frac{1}{2}\cos^4\alpha\,\Delta\kappa tE\cos\psi \qquad 2.7$$

For bi-normal curvature:

$$\Delta\sigma_{11}^{M_3} = \frac{1}{2}\cos\alpha(1+\sin^2\alpha)\,\Delta\kappa bE\sin\psi \qquad 2.8$$

For stress related to friction:

$$\sigma_{11}^{Q_1} = min\left(ER\cos^2\alpha\,\Delta\kappa\cos\psi\,, 2\left[\frac{\pi R}{2\sin\alpha\,A}(p_0+p_i)b(1+e)\mu\cos\psi\right]\right) \qquad 2.9$$

(iv)

Stress concentration factors

Integrity assessment of flexible riser with damaged tensile armour can be done by first running a FEM simulation for the load case being considered with an intact riser. Then, running the same load case, but with a number of wires broken. Stress concentration factors (SCF) can be established from the two simulations for mean and dynamic axial stress in the wires and implemented in a fatigue analysis to predict the remaining fatigue life of the riser. SCF`s in the current work are defined in **Table 2-1** where index d denotes damaged.

Table 2-1: Definition of stress concentration factors (SCF).

Stress concentration factors (SCF)		
Mean stress	SCF σ_{Q11}	$\sigma_{11\text{-}Q1}^{d}/\ \sigma_{11\text{-}Q1}$
Dynamic stress	ΔSCF $\sigma_{11\text{-}M2}$	$\sigma_{11\text{-}M2}^{d}/\ \sigma_{11\text{-}M2}$
	ΔSCF $\sigma_{11\text{-}M3}$	$\sigma_{11\text{-}M3}^{d}/\ \sigma_{11\text{-}M3}$

3 Numerical Methods in Flexible Pipe Analysis

Analytical methods for predicting stresses in tensile wires are now established. However, in the case of flexible pipe with broken wires, these methods may not be sufficient. This is because the stress concentration in wires close to the broken ones may increase, and normal forces may redistribute among the intact wires [13] . Furthermore, the assumption of constant curvature is not applicable for dynamic loading due to floater motions. Additionally, the assumptions made for wire path, geodesic curve (no friction) or loxodromic curve (infinite friction) may not be the path of the physical wires. One possibility is to use finite element models, which to a greater extent, are capable of simulating the complex dynamic load scenarios and associated layer interactions.

Originating from mechanics of solids, FEM is a numerical method which gives an approximation to the exact solution. In a finite element analysis (FEA), the object is discretized or divided into smaller simpler parts called finite elements. The elements approximate the geometry of the object by simple functions and each element contains a specific number of nodes depending on the type of element. Instead of solving equilibrium equations for the whole object as one, the displacement in each node is found. The equations describing each element are combined to form a global system of equations, which can, then, solve for the entire displacement field. The number of elements, and how well the object geometry is approximated will determine the accuracy of the analysis. Although accuracy is desirable, refining the mesh, hence increasing the number of elements and nodes, may also increase the computational effort significantly.

One of the advantages of finite element simulations is that it is capable of taking into account nonlinearities. This is necessary for analyses of flexible pipes. One type of nonlinearity is change in boundary conditions, like contact pressure, which governs the friction moment, and by extent, the pipe behaviour in bending. In addition to material nonlinearities which may be applicable, there are geometric nonlinearities which for flexible pipe arises when tensile wires enter the slip phase.

3.1 State of the art in FE modelling of flexible risers

Rupturing tensile wires is one of several possible flexible pipe failures, which may be why publications on this subject is rather limited. For intact pipes on the other hand, publications related to FEA have increased in parallel with the increase in computer performance over the last decades.

Flexible riser’s response to loads imposed by hydraulic collars are studied by R. M. De Sosa et al. [15]. Simulations are done in ANSYS, where shell elements represent all layers of the riser except for the tensile armours which are represented by three-dimensional beam elements. The carcass and pressure armour are modelled in a simplified manner as cylindrical layers with orthotropic material properties to attain the same stiffness as the real layers. Geometric material and contact nonlinearities are accounted for. Simulation results are

compared to experimental tests. The authors conclude that the results agree quite well and that the model is adequate to simulate the riser response to such loads.

A different model is developed by W. Wang and G. Chen [16], where a flexible riser under axial loading and torque loads is studied. The plastic layers are represented by shell elements, the tensile wires are represented by three-dimensional beam elements, and the carcass and pressure armour are represented by solid elements. The carcass is modelled with orthotropic material properties based on the method in [15], but isotropic material properties is assumed for the pressure armour. The contact is ensured with surface to surface elements. The results are compared to experimental results in the literature and the axial elongation is in the range of 40% larger for the FEM model. Twist due to torque, measured in the FE model, is about double the experimental results midrange of loading, but closer at the start and end of load range. The authors conclude that the model predicts torque behaviour well.

In a study on the behaviour of flexible risers subject to axial loading by S. Ren et al. [17], a highly detailed model of the carcass and pressure armour layers is proposed to realistically describe the complex geometry of these layers. All layers are represented by solid elements. The analyses are performed in Abaqus/Explicit with general contact. Penalty constraint based on Coulomb friction is used for the tangential behaviour with a friction coefficient of 0.1. Hard contact is used for the normal contact. The numerical results are compared to analytical calculations and experimental tests, and it is found that they are in good agreement. The original computational time would be 355 hours for this advanced model, but due to mass scaling, computational time is reduced to 66 hours. Although the mass scaling reduces computational time significantly, the authors do not provide much information as to which regions mass scaling is applied and how critical these regions are.

A numerical method for assessing the integrity of damaged flexible pipe is presented by G. Ji et al [6]. All layers in the flexible riser are represented by solid elements in the implicit nonlinear software MARC. Carcass and pressure armour are modelled in a simplified manner with orthotropic material properties. An automatic contact algorithm accounted for contact between all layers with a friction coefficient of 0.15. The FE model is subject to tension, internal and external pressure, and bending. Mean and dynamic stress concentration factors (SCF) for inner tensile armour with failure in two, four, and six neighbouring wires are evaluated. The effects on pipe curvature are also investigated. It is found that the curvature of riser increases when the number of broken wires increase. Accumulated time until cross section failure in a probabilistic sense is also estimated for scenarios with high and low correlation between failure events. For the first scenario, the elapsed time until failure of one wire is 6.4 years and 13.2 until failure of cross section. An additional 6.8 years until cross section failure is found for the second case.

In a study by R. M. De Sosa et al. [13], the mechanical response of a flexible pipe with broken tensile wires subject to combined tension and bending loads is analysed. The same FE model, as in [15], is used in the simulations, but the model is modified to account for one up to four broken wires in the outer tensile armour. Experimental tests are performed and deflections along the pipe and strains in outer tensile wires are measured in order to calculate

bending stiffness, and thereafter, force distribution among the wires. The authors find that the numerical and analytical predictions agree well with the results of experimental tests, and that there is a negligible decrease in pipe stiffness with increasing number of broken wires. Moreover, a redistribution of forces is found among the intact wires of the damaged layer with high stress concentration in the wires close to the broken ones. Additionally, it is found that the rupture of tensile wires does not affect the normal and transvers stresses in these wires, and that the SCFs related to tension and bending are quite close. Therefore, the authors suggest that a single SCF may be used in computing the limit loads of these structures.

3.2 Abaqus

Abaqus is a powerful nonlinear finite element software for modelling and analysis. It is widely used in both academia and industry as the general-purpose analysis program is applicable to many fields of research due to its large material modelling capability. Abaqus has no built in system of units, thus, it is important that all input data is specified in consistent units. Relevant features of Abaqus/Standard [18] are presented in the following text.

(i)

Solution sequences

A full finite element analysis is done in three stages. The first stage is the pre-processing or commonly known as modelling, in which the model is created and meshed, assigned material, element types, constraints, interactions, and boundary conditions. It is also possible to import files from other pre-processing software. The second stage is processing where stiffness is generated and modified, and the equations of the finite element problem is solved, producing an output file and log file. This is a “black box” process where the user cannot see the calculations, but it is possible to monitor the job while it is running. The log file can also be consulted to check for errors or warnings and verify that the numerical processing behaved well during solution. The third stage is post-processing, where the results in the output file are represented. Visual rendering of the result is provided in the visualization module with many display options.

(ii)

Material modelling

Generally, materials are defined by selecting material behaviour and assigning the relevant properties. The material library contains many material behaviours and cover both linear and nonlinear, isotropic and anisotropic behaviour. All types of anisotropic material properties must be given in a local coordinate system. Defining material orientation for isotropic materials can also be useful, (e. g. for tensile wires, because it makes it possible to measure stress in the lay direction of the wires). Creating orthotropic materials is easiest done by assigning engineering constants, that is, the Young’s modulus (E), shear modulus (G) and Poison`s ratio (ν) in the principal directions of the material.

(iii)

Elements and their characteristics

The extensive element library in Abaqus/standard is divided into element families. Typical families for stress analysis are continuum elements (solid), structural (shell elements, beam element, and truss elements). One of the main distinctions that separates the different element families is the geometry which they assume.

Solid elements are the standard volume elements which have least restrictions for modelling geometries. They have displacement degrees of freedom (DOF) and are more accurate than other elements if not distorted. If the structure`s thickness is significantly lesser than the other dimensions, then conventional shell elements can be used to model it. For conventional shell elements, the geometry of the body is specified at the reference surface and element thickness is defined as a section property. These elements have displacement and rotational DOF, and compared to solid elements, these generally contain a smaller number of nodes. Beam elements are applicable for slender structures. The element is a one-dimensional line element in three-dimensional space that has stiffness associated with deformation of the beam axis. That is axial elongation, bending and torsion. Truss element is a similar one-dimensional line element that have only axial stiffness. Both linear beam elements and truss elements have only two nodes, where beam has six DOF and truss has 3 DOF for each node respectively.

The behaviour of an element is characterised by five aspects:

- Family
- Degrees of freedom
- Number of nodes
- Formulation
- Integration

All elements have individual names which typically describes some of its characteristics with respect to the aspects above. Take the solid element C3D8 as an example. The first letter C denotes that it belongs to the continuum (solid) family, 3D stands for three dimensional, and 8 is the number of nodes.

DOF are the central variables computed during simulations, which may be different from one element family to another. In a stress/displacement analysis with solid elements, the DOFs are the translations, and with shell and beam elements, the rotation at each node. DOF are calculated at the nodes, and for any other location within the element, the DOFs are interpolated form the nodal values. Number of nodes in the element governs the order of interpolation. The element C3D8, which has one node in each corner, uses linear interpolation. Therefore, it is often referred to as a linear element. A solid element with mid-side nodes (C3D20) uses quadratic interpolation and therefore the term quadratic or second-order elements are used. Both elements are shown in **Figure 3-1**.

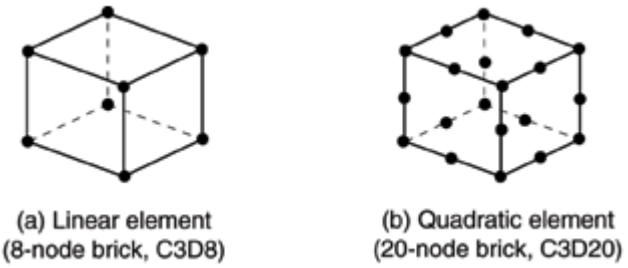

Figure 3-1: Linear and quadratic solid elements.

Element formulation is the mathematical theory describing element behaviour. Abaqus/standard uses the Lagrangian formulation for most of the stress/displacement elements, in which the elements deform with the material. Numerical techniques are used to integrate different quantities over the volume of each element. Gaussian quadrature is the technique used for most elements. Material response is assessed at each integration point in each element. Some elements have reduced integration, which is denoted with an R at the end of the element name. These elements use fewer Gaussian coordinates per element when solving the integral. One advantage of the reduced integration procedure is decreased computational time. It can also preventing shear locking which may occur for the linear full integration element. Shear locking is an issue for thin or slender structures in bending with few elements over thickness. This is because of the linear interpolation which yields constant strains through the element. The result is a significant increase in stiffness. Reduced integration may cause no straining at the integration points, leading to inaccurate solutions. This is called the hourglass effect and is most severe in linear elements. However, reduced integration elements like C3D8R and SH4 have hourglass control which address the problem by inserting an artificial stiffness to the hourglass modes.

(iv)

Solution method for nonlinear problems

A core concept in Abaqus is dividing the problem history into steps. In Abaqus/standard, a step is simply an analysis of load change from one magnitude to another. For each step, a procedure is selected which defines the type of analysis performed during the step. The different procedures can be generalized as static or dynamic analyses. In the dynamic procedures, inertia effects are considered, but not for static procedures.

Finding the exact solution to a stress/displacement problem requires an equilibrium of forces and moments at all times over any volume of the object. In FEM this requirement is reduced to a weaker form, which is to maintain equilibrium over a finite number of sections of the objects volume, in an average manner. Hence, FEM gives an approximate solution to the problem. The principal of virtual work is used to express the equilibrium statement on weak form and may be given as:

$$\int_V \boldsymbol{\sigma} : \delta\mathbf{D}\ dV = \int_S \mathbf{t}^{\mathrm{T}} \cdot \delta\mathbf{v}\, dS + \int_V \mathbf{f}^{T}\ \cdot \delta\mathbf{v}\, dV \qquad 3.1$$

The left side of the equation is the internal work rate where **σ** is the Cauchy stress matrix and **D** is the virtual strain rate. The right side of the equation is the external work rate which consist of two terms: the work done by traction forces over the surface of the volume and by body forces acting on the volume. Here, $\mathbf{t}^{\mathrm{T}}$ and $\mathbf{f}^{\mathrm{T}}$ are the transposed traction force and body force matrix, respectively. δ**v** is a velocity field representing the test function. The test function is required to have sufficient continuity and defer to any prescribed kinematic constraints, except for these requirements it is completely arbitrary. Approximations can be introduced by selecting test functions for the virtual velocity field with variations restricted to a finite number of nodal values. Compared to the alternative method, the finite difference method (FDM) where direct discretization of the derivative in the differential equation of equilibrium at a point is necessary, FEM provides a stronger mathematical basis for studying the approximation [18]. Expressing the internal work in equation 3.6 in terms of the integral over the reference volume of the virtual work rate per reference volume defined by connected pairs of stress (τ^c) and strain (ε), the equilibrium statement becomes:

$$\int_{V^0} \boldsymbol{\tau}^{c} : \delta\boldsymbol{\varepsilon}\, dV^0 = \int_S \mathbf{t}^{\mathrm{T}} \cdot \delta\mathbf{v}\, dS + \int_V \mathbf{f}^{T}\ \cdot \delta\mathbf{v}\, dV \qquad 3.2$$

Here, V^0 denotes the reference volume. Introducing the finite element interpolator on general form:

$$\mathbf{u} = \mathbf{N}_N u^N \qquad 3.3$$

Here, $\mathbf{N}_N$ is a set of interpolation functions determined by the material coordinate system and u^N are nodal variables. The subscripts and superscripts denote nodal variables, for which the summation convention is adopted. The displacement is restricted by the interpolation above to have only some spatial forms. Due to the requirements for the velocity field (δ**v),** it is required to have the same spatial form as the displacement:

$$\delta\mathbf{v} = \mathbf{N}_N \delta v^N \qquad 3.4$$

Equation 3.2 is therefore approximated by alteration over the finite selection δv^N. Associated with the virtual velocity field, the virtual rate of strain (δ**ε**) is linear in δ**v.** Therefore, the virtual strain rate can be given as:

$$\delta\boldsymbol{\varepsilon} = \boldsymbol{\beta}_N \delta v^N \qquad 3.5$$

The matrix $\boldsymbol{\beta}_N$ describes the strain variations of the kinematic variables and, generally, depends on the present location (**x**) of the point currently considered. Once the specific strain measure to be used is determined, the matrix can be derived from the interpolation functions. Without further details on how to derive the expression (details are found in [18]), but skipping to the final form:

$$\int_{V^0} \boldsymbol{\beta}_N : \boldsymbol{\tau}^c \, dV^0 = \int_S \mathbf{N}_N^T \cdot \mathbf{t} \, dS + \int_V \mathbf{N}_N^T \cdot \mathbf{f} \, dV \tag{3.6}$$

This system of nonlinear equations is the basis for displacement analysis in Abaqus/standard. Discretized and on symbolic form this can be written as:

$$F^N(u^M) = 0 \tag{3.7}$$

Here, F^N is the force component related to the N^{th} variable in the equation and u^M is the Mth variable. The essential issue is to solve equation 3.7 for u^M throughout the problem history.

In linear FEA, the stiffness matrix is constant and superposition is possible, meaning that double the load equals double the displacement. Thus, displacement can be calculated by inverting the stiffness matrix directly. In nonlinear FEA, on the other hand, double the load does not equal double displacement. Therefore, incremental solution procedures are necessary to solve for displacement. The Newton-Raphson method is the preferred numerical technique for solving nonlinear equilibrium equations because its convergence rate exceeds that of other methods (i.e. modified Newton or quasi-Newton methods). The formal description of the Newton-Raphson method is as follows. Granted that after an iteration *i*, an approximation u_i^M to the solution is found. Then, c^M_{i+1} is the solution error in equation 3.7, yielding:

$$F^N(u_i^M + c_{i+1}^M) = 0 \tag{3.8}$$

The left side of this equation can be expanded in a Taylor series based on the approximate solution (u_i^M) and the expression becomes:

$$F^N(u_i^M) + \frac{\partial F^N}{\partial u^P}(u_i^M)c_{i+1}^P + \frac{\partial^2 F^N}{\partial u^P \partial u^Q}(u_i^M)c_{i+1}^P c_{i+1}^Q + \cdots = 0 \tag{3.9}$$

As long as u_i^M is close to the real solution which also means c^M_{i+1} will be small, then all terms except the first two are negligible. This results in a linear system of equations:

$$K_i^{NP} c_{i+1}^P = -F_i^N \tag{3.10}$$

Here, K_i^{NP} is the Jacobian matrix which in addition to F_i^N is, in this order, given as:

$$K_i^{NP} = \frac{\partial F^N}{\partial u^P}(u_i^M) \tag{3.11}$$

And

$$F_i^N = F^N(u_i^M) \tag{3.12}$$

The full Jacobian matrix and how to derive it can be found in [18]. Equation 3.6 together with the Jacobian matrix makes up the basis for the Newton-Raphson incremental solution, in combination with the constitutive theories and interpolation functions specified.

4 Equivalent Properties and Orthotropic Materials

Creating a detailed FE model which describes the geometry of carcass and pressure armour layers directly would be a highly laborious task and require enormous computational effort. The complex cross section geometry and large lay angle would result in a substantial number of degrees of freedom (DOF). Therefore, a simplified model with the same axial- and bending-stiffness could be used to efficiently describe these layers, at a much lower computational cost. In a simplified model, instead of considering the complex cross section geometry of the physical carcass tendon and pressure armour tendon, a cylinder of uniform wall thickness, which is continuous over the length of cylinder, is considered. The difference between a detailed and simplified model is illustrated in **Figure 4-1**. The material assigned to these layers must have equivalent orthotropic properties in order to get the simplified model to behave like the real carcass and pressure armour. This is achieved by attaining the same stiffness and stresses for the simplified model as for the real layers. The orthotropic material properties are given to these layers by assigning engineering constants in longitudinal, radial and circumferential direction.

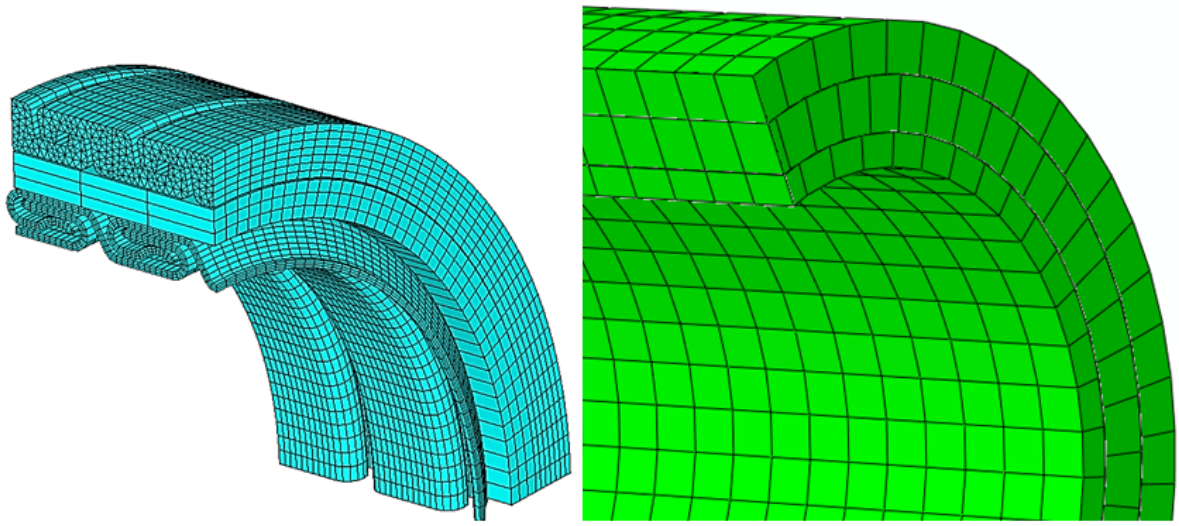

a) Detailed model. b) Simplified model.

Figure 4-1: Detailed and simplified model of carcass, internal plastic sheath and pressure armour layer.

Orthotropic materials is a subset of anisotropic materials that exhibit different properties in the three principal directions. Linear elasticity can be defined by engineering constants. That is Young's moduli, E_1, E_2, E_3, shear moduli, G_1, G_2, G_3, and Poisons ratios, ν_{12}, ν_{13}, ν_{23}. The engineering constants express the flexibility of the material according to:

$$\begin{Bmatrix} \varepsilon_{11} \\ \varepsilon_{22} \\ \varepsilon_{33} \\ \gamma_{11} \\ \gamma_{22} \\ \gamma_{33} \end{Bmatrix} = \begin{bmatrix} \frac{1}{E_1} & \frac{-v_{12}}{E_2} & \frac{-v_{31}}{E_3} & 0 & 0 & 0 \\ \frac{-v_{12}}{E_1} & \frac{1}{E_2} & \frac{-v_{32}}{E_3} & 0 & 0 & 0 \\ \frac{-v_{13}}{E_1} & \frac{-v_{23}}{E_2} & \frac{1}{E_3} & 0 & 0 & 0 \\ 0 & 0 & 0 & \frac{1}{G_{12}} & 0 & 0 \\ 0 & 0 & 0 & 0 & \frac{1}{G_{13}} & 0 \\ 0 & 0 & 0 & 0 & 0 & \frac{1}{G_{23}} \end{bmatrix} \begin{Bmatrix} \sigma_{11} \\ \sigma_{22} \\ \sigma_{33} \\ \sigma_{12} \\ \sigma_{13} \\ \sigma_{23} \end{Bmatrix} \quad 4.1$$

For a stable isotropic material, Poison`s ratio *v* must have a value between -1/2 and 0.5. Although v_{ij} has no apparent limits for orthotropic materials, the following criteria must be satisfied for an orthotropic material to achieve stability:

$$|\nu_{12}| < \sqrt{\frac{E_1}{E_2}}, \qquad |\nu_{13}| < \sqrt{\frac{E_1}{E_3}}, \qquad |\,\nu_{23}| < \sqrt{\frac{E_2}{E_3}} \quad 4.2$$

Two approaches for calculating equivalent properties for carcass and pressure armour are presented in the following sections. Both assume linear material behaviour. The first approach is developed for a simplified model where the layers are represented by shell elements. The second one is developed for a simplified model where the carcass is omitted and the pressure armour layer is represented by solid elements. Engineering constants for the simplified carcass and pressure armour layers are established according to assumptions and calculations in the respective approaches.

4.1 Approach 1

De Sosa [19] proposes a method to calculate the equivalent properties where he establish an analogy between helical tendons and orthotropic shells, which are based on the following four hypotheses:

1. Internal friction is negligible in these layers.
2. There is no interaction between the lay direction of the tendons and their normal directions.
3. The thickness of the layer is small in comparison to the internal diameter of the layer.
4. Shear effects are negligible meaning that the linear elements perpendicular to the middle plane of the structure remain straight and normal to the deflection surface of the structure after bending.

The tendons of the carcass and pressure layers are laid at angles close to 90° with internal gaps. Additionally, the thickness to diameter ratio is small enough for the layers to be considered as thin walled cylinders. De Sosa argues that this validates the four hypotheses, and as a result, the tendons can be considered as helical beams and could be modelled with 3D-beam elements. To reduce computational time, the tendons are instead represented by orthotropic shell elements. Introducing a local coordinate system (see **Figure 4-2**), the stress-strain relations are given in eq. 4.3.

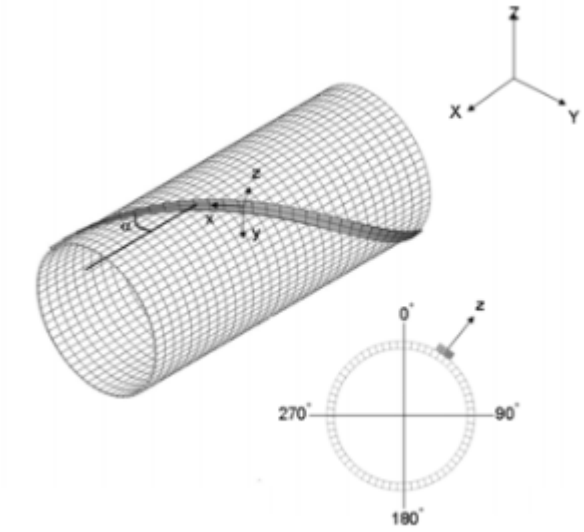

Figure 4-2: Coordinate systems.

$$\begin{cases} \sigma_{s_x} = \dfrac{E_{s_x}}{1 - v_{s_{xy}} v_{s_{yx}}} \varepsilon_{s_x} + \dfrac{E_{s_x} v_{s_{yx}}}{1 - v_{s_{xy}} v_{s_{yx}}} \varepsilon_{s_y} \\ \sigma_{s_y} = \dfrac{E_{s_y} v_{s_{xy}}}{1 - v_{s_{xy}} v_{s_{yx}}} \varepsilon_{s_x} + \dfrac{E_{s_y}}{1 - v_{s_{xy}} v_{s_{yx}}} \varepsilon_{s_y} \\ \tau_{s_{xy}} = G_{s_{xy}} \gamma_{s_{xy}} \end{cases} \quad 4.3$$

Where σ_s, τ_s, ε_s, and γ_s, are normal and shear stress at the shell surface, elongation and angular distortion, respectively. Additionally, E_s, G_s, and v_s, are the Young`s modulus, shear modulus, and Poison ratio, of the shell material, respectively. The tendons do not resist loads normal to the lay direction as claimed by hypotheses 1 and 2, therefore assuming $E_{sy} = 0$ and $v_{syx} = v_{sxy} = 0$. This leaves the stress-strain relations as:

$$\sigma_{s_x} = E_{s_x} \varepsilon_{s_x}, \qquad \sigma_{s_y} = 0, \; \tau_{s_{xy}} = G_{s_x} \gamma_{s_{xy}} \quad 4.4$$

Furthermore, based on Timoshenko and Woinowsky-Krieger`s plate theory [20], the membrane, bending, and torsional stiffness of the equivalent orthotropic shell are given by:

$$(EA)_s = h_s E_{s_x}, (EI)_s = \left(\frac{H_s^3}{12}\right) E, (GJ)_s = \left(\frac{h_s^3}{3}\right) G_{s_{xy}} \quad 4.5$$

Where h_s is the shell thickness. Again based on Timoshenko and Woinowsky-Krieger`s plate theory [20], the axial, bending, torsional stiffness of a helical tendon is given by:

$$(EA)_t = \left(\frac{An_t}{L_p}\right) E, (EI)_t = \left(\frac{I_{eq} n_t}{L_p}\right) E, (GJ)_t = \left(\frac{Jn_t}{L_p}\right) G \quad 4.6$$

Where E and G are the Young's modulus and the shear modulus of the tendon material, n_t is the number of tendons of said layer, and A, J, and L_p, are the cross section area, torsion constant, and pitch length of the tendon, respectively. Pitch length can be expressed as:

$$L_p = \frac{2 * \pi * R}{\tan(\alpha)} \quad 4.7$$

Where α is the lay angle of the tendon and R is the mean radius of the layer, which is given by:

$$R = \frac{d_i}{2} + \frac{h}{2} \quad 4.8$$

Where d_i is the inner radius of the layer and t is the thickness of the layer. I_{eq} is the equivalent second moment of area, given by:

$$I_{eq} = 12 * n_t * \frac{I_y^2}{L_p} * \frac{1 - v^2}{h^3} \quad 4.9$$

Where I_y is the second area moment about the weakest axis of the tendon`s cross section and *v* is the Poison ratio of the material. The equivalent material and geometric properties of the orthotropic shells are found by setting eq. 4.5 equal to eq. 4.6:

$$h_s = \sqrt{12 * \frac{I_{eq}}{A}}, E_{s_x} = \left(\frac{n_t * A}{L_p * h_s}\right) * E, \; G_{s_{xy}} = \left(\frac{3 * n_t * J}{L_p * h_s^3}\right) * G \quad 4.10$$

4.2 Approach 2

In Jørgensen`s work [21], the pressure armour layer is represented by a simplified model consisting of solid elements and embedded rebar elements. Methods derived from mechanics of solids are employed to investigate the stiffness of the pressure armour and calculate the equivalent properties of the orthotropic material. The approach is based on the following hypotheses:

1) Contact and friction between the windings are negligible.
2) Shear effects in the layer are negligible as it is a rather slender structure.

(i)

Axial stiffness

According to hypothesis 1, the pressure armour could be considered as a helical spring with low pitch. A tensile load would create both a bending and torsional moment, but due to the low tendon pitch, the bending moment is negligible. Consequently, a pure torsional moment is considered governing the axial stiffness of the pressure armour:

$$T = FR \tag{4.11}$$

Where T, F, R, are the torsional moment, tensile force, and radius, respectively. The torsional moment will cause a cross section rotation and an axial elongation of the structure. St. Venant`s theory states the rotation as:

$$d\phi = \frac{T}{GI_p} ds = \frac{FR}{GI_p} ds \tag{4.12}$$

Where G and I_p are the material shear modulus and torsional second area moment of the tendon cross section. In addition, the elongation can be stated as:

$$d\delta = d\phi R = \frac{T}{GI_p} R ds = \frac{FR^2}{GI_p} ds \tag{4.13}$$

As the elongation does not change along the tendon, this expression becomes:

$$\delta = \frac{FR^2}{GI_p} R\theta = \frac{FR^3}{GI_p} 2\pi n \tag{4.14}$$

Where $2\pi n=\theta$ is the total angle of the tendon along the structure and n is the number of turns.

(ii)

Radial stiffness

Considering the radial stiffness, an expression for radial displacement of the pressure armour due to internal pressure loading (p) can be derived by looking at a cylindrical cross section representing a single armour strip with dimensions: radius R, width b, and cross section area A. Due to symmetry of both the cross section and the loading, the hoop stress, σ, can be found from equilibrium:

$$2\sigma A = 2pRb$$

$$\sigma = \frac{pRb}{A} \qquad 4.15$$

By inserting Hook`s law, the strain can be expressed as:

$$\epsilon = \frac{pRb}{EA} \qquad 4.16$$

Where E is the Young`s modulus of the material. Now, the radial displacement can be expressed with help of the strain expression. The circumference, L=2πR, will be altered when an internal pressure is applied. Due to the radial displacement (δ) caused by the pressure load, the circumference can be stated as L+ΔL=2π(R+ δ). As a result, the strain can be given as:

$$\epsilon = \frac{\Delta L}{L} = \frac{2\pi\delta}{2\pi R} = \frac{\delta}{R} \qquad 4.17$$

Equalling equation 4.16 and 4.17, an expression for displacement as a function of pressure is derived:

$$\frac{\delta}{R} = \frac{pRb}{EA}$$

$$\delta = \frac{pR^2b}{EA} \qquad 4.18$$

(iii)

Bending stiffness

In the process of assessing the bending stiffness of the pressure armour, the tendon will be considered a beam with curved shape and mean radius R, axial stiffness EA, and bending stiffness EI. Furthermore, this process will consist of calculating the rotations, deflections and bending moment with use of the unit load method. In accordance with hypothesis 2, this structure is slender, shear deformation is considered negligible, but axial and bending

deformations are accounted for. On this basis, deflections can be calculated from the following expression for virtual work [22]:

$$1 * \delta = \int_0^L \frac{N\tilde{N}}{EA} ds + \int_0^L \frac{M\tilde{M}}{EI} ds \qquad 4.19$$

Where δ can either be the rotation or the deflection at an arbitrary point of the curved beam. M̃ is the bending moment due to dummy unit load at the point considered and M is the bending moment experienced by the beam, caused by the physical load. Similarly, Ñ is the axial load due to a dummy unit load at the point considered and N is the axial force experienced by the beam, caused by the physical load. The symmetric geometry makes it possible to only analyse half the cross section by introducing the boundary conditions as in **Figure 4-3**. The beam is statically indeterminate; therefore a statically determinate structure is chosen (see **Figure 4-4**), to able the calculation of bending moment diagram. To calculate the unknown rotations in A and B, the reaction moments are assumed unknown and then solved for by establishing zero rotation in these points. The conventions listed below are be used in the calculations:

- Rotations are positive in the clockwise direction.
- A bending moment is positive when it gives tension on the inside of the arch.
- Compression is negative and tension is positive.

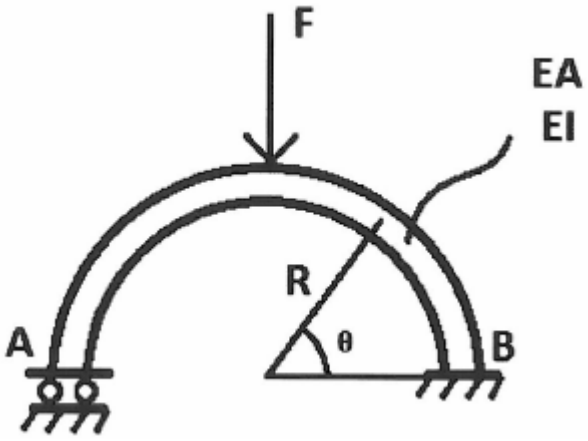

Figure 4-3: Curved beam with fixed and roller support.

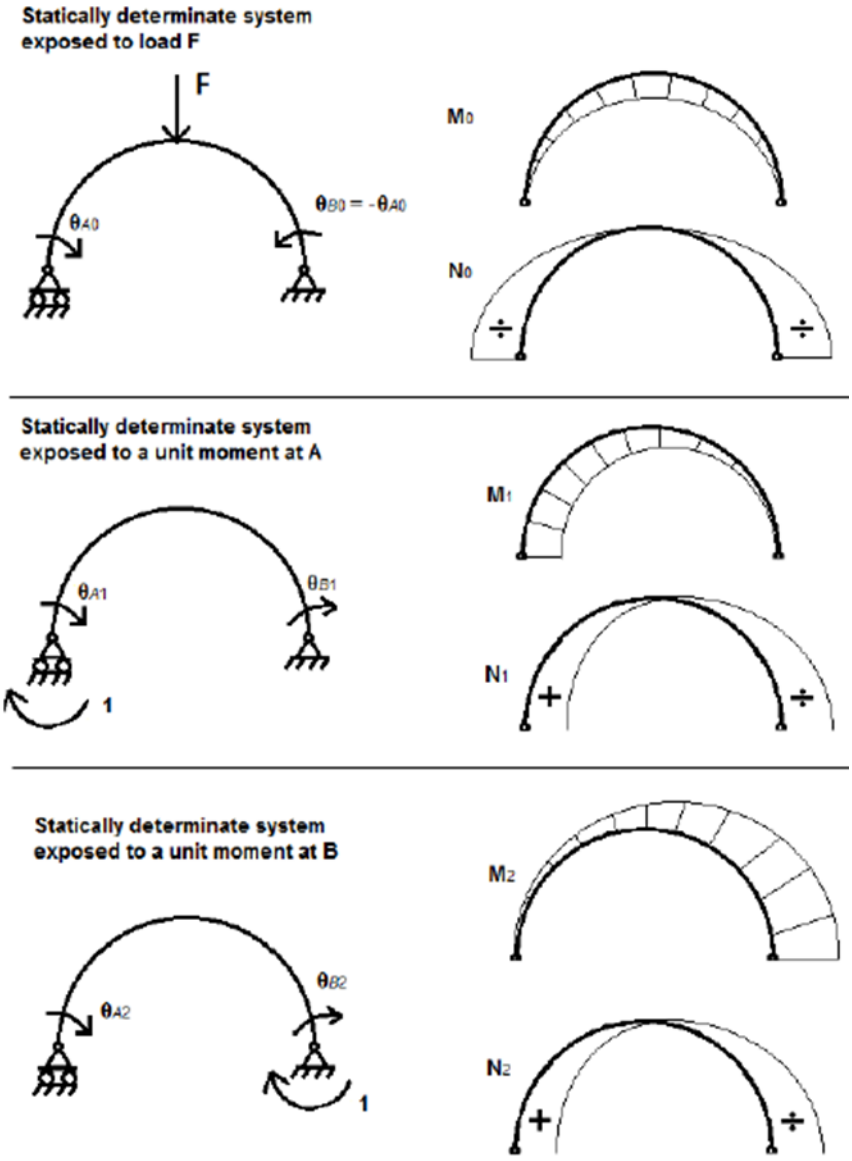

Figure 4-4: Statically determinate curved beam and corresponding bending moment diagrams.

From equilibrium the axial force and bending moment of the beam caused by the load F, and additionally, the dummy moments in point A and B are found:

$$
\begin{aligned}
M_0 &= \frac{FR}{2}(1 - |cos\theta|) \\
N_0 &= -\frac{F}{2}|cos\theta| \\
M_1 &= \frac{1}{2}(1 - cos\theta) \\
N_1 &= -\frac{1}{2R}cos\theta \\
M_2 &= \frac{-1}{2}(1 + cos\theta) \\
N_2 &= -\frac{1}{2R}cos\theta
\end{aligned}
\qquad 4.20
$$

The rotation in point A, θ_{A0}, due to force F is found next. As the axial force term cancels out due to equal magnitude and opposite signs, eq. 4.19 is reduced to:

$$\theta_{A0} = \int_0^L \frac{M\widetilde{M}}{EI} ds$$

$$= \frac{FR}{4EI} \int_0^{\pi} (1 - |cos\theta|)\,(1 - cos\theta) R\, d\theta$$

$$= \frac{FR^2}{4EI} \left\{ \int_0^{\frac{\pi}{2}} (1 - cos\theta)^2 d\theta + \int_{\frac{\pi}{2}}^{\pi} (1 + cos\theta)(1 - cos\theta)\, d\theta \right\}$$

$$= \frac{FR^2}{4EI} \left\{ \int_0^{\frac{\pi}{2}} 1 - 2cos\theta + \cos^2\theta \; d\theta + \int_{\frac{\pi}{2}}^{\pi} 1 - \cos^2\theta \, d\theta \right\} \qquad 4.21$$

$$= \frac{FR^2}{4EI} \left\{ \left[\theta - 2sin\theta + \frac{1}{2} sin\theta \; cos\theta + \frac{\theta}{2} \right]_0^{\frac{\pi}{2}} + \left[\theta - \frac{1}{2} sin\theta \; cos\theta - \frac{\theta}{2} \right]_{\frac{\pi}{2}}^{\pi} \right\}$$

$$= \frac{FR^2}{4EI} \left\{ \frac{\pi}{2} - 2 + \frac{\pi}{4} + \pi - \frac{\pi}{2} - \left(\frac{\pi}{2} - \frac{\pi}{4} \right) \right\}$$

$$= \frac{FR^2}{4EI} (\pi - 2) = \frac{FR^2}{2EI} \left(\frac{\pi}{2} - 1 \right) = -\theta_{B0}$$

As a result of the symmetrical geometry, the relation $\theta_{A0} = -\theta_{B0}$ must be true. In the following calculations, a unit moment is applied to point A to find the corresponding rotation, in point A:

$$\theta_{A1} = \int_0^{\pi} \frac{M_1^2}{EI} R d\theta + \int_0^{\pi} \frac{N_1^2}{EA} R\, d\theta$$

$$= \frac{R}{EI} \int_0^{\pi} \frac{1}{4} (1 - cos\theta)^2\, d\theta + \frac{R}{EA} \int_0^{\pi} \left(\frac{1}{2R} \right)^2 \cos^2\theta \, d\theta$$

$$= \frac{R}{4EI} \left[\theta - 2sin\theta + \frac{1}{2} sin\theta \cos\theta + \frac{\theta}{2} \right]_0^{\pi} + \frac{R}{4EAR} \left[\frac{1}{2} sin\theta \cos\theta + \frac{\theta}{2} \right]_0^{\pi} \qquad 4.22$$

$$= \frac{R}{4EI} \left(\pi + \frac{\pi}{2} \right) + \frac{1}{4EAR} \frac{\pi}{2} = \frac{3\pi R}{8EI} + \frac{\pi}{8EAR}$$

Now for the rotation in point B, due to the same dummy load in point A:

$$\begin{aligned}\theta_{B1} &= \int_0^{\pi} \frac{M_1 M_2}{EI} R d\theta + \int_0^{\pi} \frac{N_1 N_2}{EA} R\, d\theta \\ &= \frac{-R}{4EI} \int_0^{\pi} (1 - cos\theta)(1 + cos\theta)\, d\theta + \frac{\pi}{8EAR} \\ &= \frac{-R}{4EI} \left[\theta - \frac{1}{2} sin\theta\, cos\theta - \frac{\theta}{2}\right]_0^{\pi} + \frac{\pi}{8EAR} \\ &= \frac{-R}{4EI}\left(\pi - \frac{\pi}{2}\right) + \frac{\pi}{8EAR} = -\frac{\pi R}{8EI} + \frac{\pi}{8EAR}\end{aligned} \qquad 4.23$$

Because $N_1 = N_2$, the last term in eq. 4.22 and eq. 4.23 are equal. In addition to this, the symmetry of the curved beam leads to the following relations:

$$\begin{aligned}\theta_{A2} &= \theta_{B1} \\ \theta_{B1} &= \theta_{A1}\end{aligned} \qquad 4.24$$

Next, the moments in point A and B can be calculated by ensuring zero rotation. Considering the symmetry of the curved beam, the reaction moments must have the same magnitude but act in opposite directions. Solving the equation for rotation in point A with respect to the moment:

$$\begin{aligned}&\theta_{A0} + X_1\theta_{A1} + X_2\theta_{A2} = 0 \\ \rightarrow\ &\theta_{A0} + X_1\theta_{A1} - X_1\theta_{A2} = 0 \\ \rightarrow\ &\theta_{A0} + X_1(\theta_{A1} - \theta_{A2}) = 0 \\ \rightarrow\ &X_1 = \frac{-\theta_{A0}}{\theta_{A1-}\theta_{A2}} \\ &= \frac{-\frac{FR^2}{2EI}\left(\frac{\pi}{2} - 1\right)}{\frac{\pi}{8EAR} + \frac{3\pi R}{8EI} - \left(\frac{\pi}{8EAR} - \frac{\pi R}{8EI}\right)} \\ &= -\frac{FR}{\pi}\left(\frac{\pi}{2} - 1\right)\end{aligned} \qquad 4.25$$

The bending stiffness EI and axial stiffness EA has disappeared from the expression, proving the distribution of bending moment is not related to stiffness of the cross section. Now that the rotations and moments are known, the total bending moment of the beam can be established:

$$
\begin{aligned}
M &= M_0 + X_1 M_1 + X_2 M_2 \\
&= M_0 + X_1 (M_1 - M_2) \\
&\quad = \frac{FR}{2}(1 - |cos\theta|) - \frac{FR}{\pi}\left(\frac{\pi}{2} - 1\right)\left(\frac{1}{2}(1 - cos\theta)\right. \\
&\quad\quad \left. + \frac{1}{2}(1 + cos\theta)\right. \\
&= \frac{FR}{2}(1 - |cos\theta|) - \frac{FR}{\pi}\left(\frac{\pi}{2} - 1\right) \\
&\quad\quad = \frac{FR}{\pi}\left(1 - \frac{\pi}{2}|cos\theta|\right)
\end{aligned}
\qquad 4.26
$$

In a similar fashion, the total axial force, N, can be calculated. As previously mentioned, N_1=N_2, and N becomes:

$$N = N_0 + X_1 N_1 + X_2 N_2 = N_0 + X_1 (N_1 - N_2) = N_0 \qquad 4.27$$

With the total bending moment and axial force established, the deflection caused by the applied load F can finally be found with eq. 4.19:

$$
\begin{aligned}
\delta &= \int_0^L \frac{M\widetilde{M}}{EI} ds + \int_0^L \frac{N\widetilde{N}}{EA} ds \\
&= \frac{2}{EI}\int_0^{\frac{\pi}{2}} \frac{FR}{\pi}\left(1 - \frac{\pi}{2}cos\theta\right)\frac{R}{\pi}\left(1 - \frac{\pi}{2}cos\theta\right) R\, d\theta \\
&\quad\quad + \frac{2}{EA}\int_0^{\frac{\pi}{2}} \frac{-F}{2} cos\theta \left(\frac{-1}{2}\right) cos\theta\, R\, d\theta \\
&= \frac{2FR^3}{\pi^2 EI}\int_0^{\frac{\pi}{2}} 1 - \pi\, cos\theta \\
&\quad + \frac{\pi^2}{4}\cos^2\theta\, d\theta + \frac{FR}{2EA}\int_0^{\frac{\pi}{2}} \cos^2\theta\; d\theta \\
&= \frac{2FR^3}{\pi^2 EI}\left[\theta - \pi\; sin\theta + \frac{\pi^2}{4}\left(\frac{1}{2} sin\theta \cos\theta + \frac{\theta}{2}\right)\right]_0^{\frac{\pi}{2}} \\
&\quad + \frac{FR}{2EA}\left[\frac{1}{2} sin\theta \cos\theta + \frac{\theta}{2}\right]_0^{\frac{\pi}{2}} \\
&= \frac{2FR^3}{\pi^2 EI}\left(\frac{\pi}{2} - \pi + \frac{\pi^2}{4}\frac{\pi}{4}\right) + \frac{FR}{2EA}\frac{\pi}{4} \\
&= \frac{FR^3}{\pi EI}\left(\frac{\pi^2}{8} - 1\right) + \frac{\pi}{8}\frac{FR}{EA}
\end{aligned}
\qquad 4.28
$$

(iv)

Equivalent properties

The properties of the orthotropic material is defined by Young`s modulus and shear modulus in the three principal directions of a cylindrical coordinate system. The shear modulus is assigned the actual value of 80 GPa in all directions. Young's modulus in the longitudinal direction is set to a very small value as the axial stiffness of the pressure armour is considered negligible (hypothesis 1). In radial direction, the actual value of 205 GPa is used. Young's modulus in the circumferential direction can be found by considering the previously established radial stiffness and bending stiffness.

Looking at one strip of the real pressure armour layer and a simplified model as shown in figure 4. In the simplified model, the width of the ring is equal to the pitch of the real pressure armour, L_p. Axial stiffness of the real pressure armour is written as $(EA)_0$, and for the simplified model it can be stated as:

$$(EA)_0 = E_1 L_p t + E_0 A_{rebar} \qquad 4.29$$

Where E_0 is the real Young's modulus, A_0 is the cross section area of the pressure armour strip and t is the thickness of the layer. E_1 is the equivalent Young`s modulus in the circumferential direction of the simplified model, and A_{rebar} is the cross section area of the rebar elements (see **Figure 4-5**).

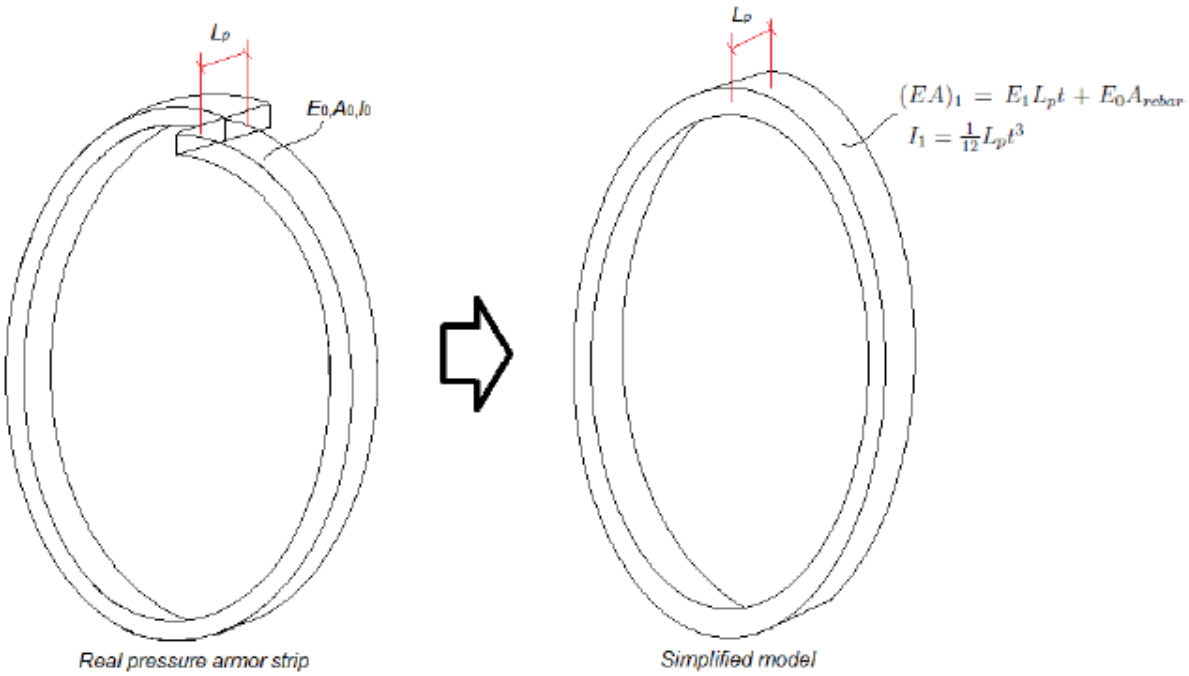

Figure 4-5: Real pressure armour strip and simplified model.

Comparing the deflection of the real pressure armour strip and the simplified model subjected to the same loading:

$$\delta_0 = \delta_1 \tag{4.30}$$

Where δ_0 is deflection of the physical armour strip and δ_1 is deflection of the simple model. Inserting the expression for deflection caused by internal pressure (eq. 4.18) into eq. 4.30, an expression for rebar area per pitch can be found:

$$\begin{aligned} p\frac{R^2 L_p}{E_0 A_0} &= p\frac{R^2 L_p}{E_1 L_p t + E_0 A_{rebar}} \\ \rightarrow E_1\left(L_p t + \frac{E_0}{E_1}A_{rebar}\right) &= E_0 A_0 \\ \rightarrow A_{rebar} &= A_0 - L_p t\frac{E_1}{E_0} \end{aligned} \tag{4.31}$$

Where p is an arbitrary pressure. The expression for deflection due to bending (eq. 4.28) can be used to find the equivalent Young`s modulus, E_1:

$$\begin{aligned} &\frac{FR^3}{\pi E_0 I_0}\left(\frac{\pi}{8}-\frac{1}{\pi}\right)+\frac{\pi}{8}\frac{FR}{E_0 A_0} = \frac{FR^3}{\pi E_1 I_1}\left(\frac{\pi}{8}-\frac{1}{\pi}\right)+\frac{\pi}{8}\frac{FR}{E_1 L_p t + E_0 A_{rebar}} \\ \rightarrow &\frac{FR^2}{E_0 I_0}\left(\frac{\pi}{8}-\frac{1}{\pi}\right)+\frac{\pi}{8}\frac{1}{E_0 A_0} = \frac{R^2}{E_1 I_1}\left(\frac{\pi}{8}-\frac{1}{\pi}\right)+\frac{\pi}{8}\frac{1}{E_1 L_p t + E_0\left(A_0 - L_p t\frac{E_1}{E_0}\right)} \\ \rightarrow &\frac{R^2}{E_0 I_0}\left(\frac{\pi}{8}-\frac{1}{\pi}\right)+\frac{\pi}{8}\frac{1}{E_0 A_0} = \frac{R^2}{E_1 I_1}\left(\frac{\pi}{8}-\frac{1}{\pi}\right)+\frac{\pi}{8}\frac{1}{E_0 A_0} \\ &\rightarrow E_1 = E_0\frac{I_0}{I_1} \end{aligned} \tag{4.32}$$

Where I_0 is the second area moment with respect to the weakest axis of the pressure armour and I_1 is the second area moment of the simplified model, which is given by:

$$I_1 = \frac{1}{12}L_p t^3 \tag{4.33}$$

4.3 Formulas for evaluation of equivalent properties

The equivalent properties calculated with approach 1 and 2 should be evaluated to see if they are suited to represent the complex geometry of the carcass and pressure armour layers. One way to evaluate approach 1 is by applying an internal pressure load to the FE model of the carcass and pressure armour layers and comparing the hoop stress to results from analytical equations. The presence of rebar in the layers of approach 2 make hoop stress values incorrect. An alternative validation method is to compare the radial displacement between corresponding layers based approach 1 and 2, assuming hoop stress values for approach 1 is sufficiently close to the analytical ones. Lamé's equations could be used to calculate the analytical hoop stress:

$$\begin{aligned} \sigma_{rr} &= A - \frac{B}{r^2} \\ \sigma_{\theta\theta} &= A + \frac{B}{r^2} \end{aligned} \tag{4.34}$$

Where σ_{rr} represent the radial stress and $\sigma_{\theta\theta}$ represent the hoop stress of the cylinder wall. A and B are unknown constants, and r is the radius. The following boundary conditions are applied:

$$\begin{aligned} r = a\text{: } \sigma_{rr} &= -P_i \\ r = b\text{: } \sigma_{rr} &= 0 \end{aligned} \tag{4.35}$$

Where *a* is the inner radius of the layer, b is the outer radius of the layer, and P_i is the internal pressure. The constants A and B are found by applying the boundary conditions:

$$\begin{aligned} \sigma_{rr} = 0 \rightarrow\ A &= \frac{B}{b^2} \\ \sigma_{rr} = -P_i \rightarrow -P_i = \frac{B}{b^2} - \frac{B}{a^2} &\rightarrow B = P_i \frac{b^2 a^2}{b^2 - a^2} \end{aligned} \tag{4.36}$$

Now A can be expressed as:

$$A = P_i \frac{b^2 a^2}{b^2 - a^2} \frac{1}{b^2} = P_i \frac{a^2}{b^2 - a^2} \tag{4.37}$$

Considering hoop stress at the inner radius:

$$\sigma_{\theta\theta}(r = a) = \ A + \frac{B}{a^2} = P_i \frac{a^2}{b^2 - a^2} \left(1 + \frac{b^2}{a^2}\right) \tag{4.38}$$

5 Methodology

This chapter intends to describe the process of creating the FE models in terms of calculating the equivalent material properties, modelling the riser with different elements and boundary conditions, in addition to defining a contact formulation that render good convergence behaviour, but at the same time can realistically describe layer interactions.

The FE models in the current work are based on the physical 2.5 inch flexible riser used in a study by De Sosa [23]. Material density and dimensions of the local carcass cross section are not provided in De Sosa`s paper. The material densities were found online, here [24] and here [25]. Dimensions of the local carcass cross section are found in the work of J.A. Witz [8], where a similar 2.5 inch riser is studied. All relevant data for the riser is presented in **Table 5-1**.

Table 5-1: Riser data.

No.	Layer description	I.D. mm	Th. mm	Lay angle	Areamm^2	I_y mm^4
1	Interlocked carcass, 1 tendon	63.5	3.5	+87.6°	19.6	23.1
2	Internal plastic sheath	70.5	5	-	-	-
3	Zeta-clip, 2 tendons	80.5	6.2	+85.6°	54.1	173.4
4	Anti-wear tape	92.9	2	-	-	-
5	Tensile armour, 2.5x8, 32 wires	96.9	2.5	+30.0°	-	-
6	Anti-wear	101.9	1.5	-	-	-
7	Tensile armour, 2.5x8, 34 wires	104.9	2.5	-30.0°	-	-
8	Fabric tape	109.9	0.5	-	-	-
9	Outer plastic sheath	110.9	5	-	-	-

Material	Density
Steel	7850 kg/m^3
Polyamide 11	1040 kg/m^3

Axial stiffness (testing in [13])	153 MNmm/mm

Carcass	Local cross section dimensions
Strip length	28mm
Strip thickness	0.7mm

5.1 Calculated equivalent properties

Equivalent properties are calculated for carcass and pressure armour based on approach 1 and 2 (ref. section 4). The calculations are presented step by step for both carcass and pressure armour layer according to the respective approaches.

(i)

Approach 1 - carcass

The torsional constant, J, is calculated by first approximating tendon cross section as a circular thin tube with assumed circumference equal to the length of carcass tendon strip, yielding the radius:

$$2\pi * r = 28mm \rightarrow r = \frac{28}{2 * \pi} = 4.4563mm$$

Then the torsion constant, J [26], may be expressed as:

$$J = \frac{2}{3}\pi * r * t^3 = \frac{2}{3}\pi * 4.4563mm * (0.7mm)^3 = 3.2013mm^4$$

Mean radius of layer:

$$R = \frac{63.5mm}{2} + \frac{3.5mm}{2} = 33.5mm$$

Pitch length of layer:

$$L_p = \frac{2 * \pi * 33.5mm}{\tan(87.6°)} = 8.8220mm$$

Equivalent second moment of area:

$$I_{eq} = 12 * 1 * \frac{(23.1mm^4)^2}{8.8220mm} * \frac{1 - 0{,}3^2}{(3.5mm)^3} = 15.4055mm^4$$

Equivalent shell thickness:

$$h_s = \sqrt{12 * \frac{15.4055mm^4}{19.6mm^2}} = 3.0711mm$$

Equivalent Young`s modulus in lay direction of tendon:

$$E_{s_x} = \left(\frac{1 * 19.6mm^2}{8.8220mm * 3.0711mm}\right) * 205000\ MPa = 148303\ MPa$$

In the circumferential direction this value is reduced to:

$$148303 \sin(87.6) = 148173\ MPa$$

Equivalent Shear modulus:

$$G_{s_{xy}} = \left(\frac{3 * 1 * 3.2013mm^4}{8{,}8220mm * (3.0711mm)^3}\right) * 80000\ MPa = 3007\ MPa$$

(ii)

Approach 1 - Pressure armour

The torsion constant, J, is calculated by approximating the tendon cross section as a solid rectangular shape, yielding the tendon width:

$$w * h = 54.1mm^2 \rightarrow w = \frac{54.1mm^2}{6.2mm} = 8.7258mm$$

Then, considering β =0.196 for w/h=1.5 [26], the torsional constant, J, can be given as:

$$J \approx \beta * w * h^3 = 0.196 * 8.7258mm * (6.2mm)^3 = 407.6021mm^4$$

Mean radius of layer:

$$R = \frac{80.5mm}{2} + \frac{6.2mm}{2} = 43.35mm$$

Pitch length of layer:

$$L_p = \frac{2 * \pi * 43.35mm}{\tan(85.6°)} = 20.9582mm$$

Equivalent second moment of area:

$$I_{eq} = 12 * 2 * \frac{(173.4mm^4)^2}{20.9582mm} * \frac{1 - 0.3^2}{(6.2mm)^3} = 131.4685mm^4$$

Equivalent shell thickness:

$$h_s = \sqrt{12 * \frac{131.4685mm^4}{54.1mm^2}} = 5.4001mm$$

Equivalent Young`s modulus in lay direction of tendon:

$$E_{s_x} = \left(\frac{2 * 54.1mm^2}{20.9582mm * 5.4001mm}\right) * 205000\ MPa = 195986\ MPa$$

In the circumferential direction this value is reduced to:

$$195986 \sin(85.6) = 195408\ MPa$$

Equivalent Shear modulus:

$$G_{s_{xy}} = \left(\frac{3 * 2 * 407.6021mm^4}{20.9582mm * (5.4001mm)^3}\right) * 80000\ MPa = 59281\ MPa$$

(iii)

Approach 2 – Carcass

Pitch length, L_p, of carcass based on outer radius, is given as:

$$L_p = 2\pi \frac{R}{\tan(87.6)} = 2\pi \frac{\left(\frac{70.5}{2}\right)}{\tan(87.6)} = 9.283mm$$

Based on the second moment of inertia found in De Sosa`s paper, 23.1mm$^4$, the equivalent Young`s modulus for the carcass becomes:

$$E_1 = E_0 \frac{I_0}{I_1} = 205000 \frac{23.1}{\frac{1}{12} 9.283 \cdot 3.5^3} = 142776\ MPa$$

Furthermore, the rebar area becomes:

$$A_{rebar} = 19.6 - 9.283 \cdot 3.5 \cdot \frac{142776}{205000} = -3.028mm^2$$

This value is negative and does not seem reasonable. De Sosa`s paper [23] does not show the calculation of second moment of inertia nor does it state over which axis it is taken. As

mentioned earlier, Witz`s paper [8] provides more detailed data on a quite similar 2.5 inch flexible pipe. The second moment of inertia from Witz`s paper, 20mm^4 (about the weak axis) inserted into the expression for equivalent Young`s modulus results in:

$$E_1 = E_0 \frac{I_0}{I_1} = 205000 \frac{20}{\frac{1}{12} 9.283 \cdot 3.5^3} = 123615\ MPa$$

In extent, yielding the following value for rebar area:

$$A_{rebar} = 19.6 - 9.283 \cdot 3.5 \cdot \frac{123615}{205000} = 0.00823 mm^2$$

The rebar area per millimetre is then:

$$A_{rebar} = \frac{0.00823}{9.283} = 8.378 \cdot 10^{-4} \frac{mm^2}{mm}$$

This value is rather small but it is positive. This equivalent properties approach was originally used for a FE model containing pressure armour, but not the carcass. It is therefore decided to consider the calculated values for pressure armour before a conclusion is made.

(iv)

Approach 2 - Pressure armour

Pitch length of the pressure armour is:

$$L_p = 2\pi \frac{R}{\tan(85.6)} = 2\pi \frac{\left(\frac{92.9}{2}\right)}{\tan(85.6)} = 22.457 mm$$

Based on the moment of inertia found in De Sosa`s paper [23], 23.1mm$^4$, equivalent Young`s modulus for pressure armour becomes:

$$E_1 = E_0 \frac{I_0}{I_1} = 205000 \frac{173.4}{\frac{1}{12} 22.457 \cdot 6.2^3} = 79700\ MPa$$

And in extent, the rebar area is given as:

$$A_{rebar} = 54.1 - 22.457 \cdot 6.2 \cdot \frac{79700}{205000} = -0.0312 mm^2$$

Similar to the carcass, the value for rebar area in the pressure armour is negative. Second moment of area from Witz`s paper [8], 100mm$^4$, is inserted into the expression for equivalent Young`s modulus, yielding:

$$E_1 = E_0 \frac{I_0}{I_1} = 205000 \frac{100}{\frac{1}{12} 22.457 \cdot 6.2^3} = 45963\ MPa$$

Furthermore, the new equivalent Young`s modulus is used for the expression for rebar area:

$$A_{rebar} = 54.1 - 22.457 \cdot 6.2 \cdot \frac{45963}{205000} = 22.883 mm^2$$

The rebar area per millimetre is then:

$$A_{rebar} = \frac{22.883}{22.457} = 1.019 \frac{mm^2}{mm}$$

The second value looks much more reasonable. To validate the moment of inertia from Witz`s paper, the difference between physical cross section area of pressure armour tendon and rebar area, in the current work and in Thorsen`s work [21] could be compared. Difference in the present work:

$$\frac{22.883}{54.1} = 0.423$$

And difference in Thorsen`s work:

$$\frac{19.91}{53.1} = 0.375$$

Difference between the two differences:

$$0.423 - 0.375 = 0.048$$

The difference in this work compared to Thorsen`s work is less than 5% which is sufficiently close to validate the chosen moment of inertia.

(v)

Poison`s ratios

As mentioned previously, to achieve a stable orthotropic material, the absolute value of the Poison`s coefficients must satisfy the criteria in section 4. In the following calculations, the material direction one, two and three are in the longitudinal, circumferential and radial direction of the riser, respectively.

(a) Approach 1- carcass:

$$|\nu_{12}| < \sqrt{\frac{100}{148173}} = 0.026, |\nu_{13}| < \sqrt{\frac{100}{148173}} = 0.026, |\nu_{23}| < \sqrt{\frac{148173}{148173}} = 1$$

(b) Approach 1- pressure armour:

$$|\nu_{12}| < \sqrt{\frac{100}{195408}} = 0.023, |\nu_{13}| < \sqrt{\frac{100}{195408}} = 0.023, |\nu_{23}| < \sqrt{\frac{195408}{195408}} = 1$$

(c) Approach 2- carcass:

$$|\nu_{12}| < \sqrt{\frac{100}{123615}} = 0.028, |\nu_{13}| < \sqrt{\frac{100}{123615}} = 0.028, |\nu_{23}| < \sqrt{\frac{123615}{123615}} = 1$$

(d) Approach 2- pressure armour:

$$|\nu_{12}| < \sqrt{\frac{100}{45963}} = 0.047, |\nu_{13}| < \sqrt{\frac{100}{45963}} = 0.047, |\nu_{23}| < \sqrt{\frac{45963}{45963}} = 1$$

5.2 General modelling

Three models are developed to describe the flexible riser. An overview of the models and elements used for each layer in the respective models are shown in **Table 5-2** where the elements containing equivalent properties are marked by an asterisk. Model 1 is not analysed. However, it is included in this section, because it could be a very computationally effective model to utilise in integrity assessment of flexible risers with damaged tensile wires. Abaqus is used to create and mesh the models in the current work and all elements are three-dimensional.

Table 5-2: Overview of the different FE models and the elements used for each layer.

Component	Model 1	Model 2	Model 3
Tensile wire	Beam	Solid	Solid
Anti-wear sheath	Shell	Shell	Solid
carcass	Shell*	Shell*	Solid*
Internal sheath	Shell	Shell	Solid
Pressure armour	Shell*	Shell*	Solid*
External sheath	Shell	Shell	Solid

Dimensions and material properties

The length of the FE models is 1200mm, which is equal to approximately two pitches of the outer tensile armour (ref eq. 4.7). Each layer of the riser is modelled separately, except for the fabric tape and outer plastic sheath. These two layers are merged into one layer to simplify the models. The equivalent properties are based on approach 1 in all three FE models and dimensions are adjusted accordingly. However, equivalent properties approach 2 could also be used. **Table 5-3** shows the dimensions of each layer in addition to the material properties of the isotropic materials that are used in the analyses. Equivalent material properties used in the simplified carcass and pressure armour are shown in **Table 5-4**. SI units with millimetres are consistently used for all input data (see **Table 5-5**).

Table 5-3: Internal diameter and layer thickness based on approach 1 and isotropic material properties.

No.	Layer description	I.D. mm	Th. mm	E MPa	*v*
1	Interlocked carcass	64.36	3.07	-	-
2	Internal plastic sheath	70.5	5.80	345	0.3
3	Pressure armour Z-profile	82.10	5.40	-	-
4	Anti-wear	92.90	2.00	345	0.3
5	Inner tensile 32×(2.5mm×8mm)	96.9 (49.7)*	2.50	205000	0.3
6	Anti-wear	101.9	1.50	345	0.3
7	Outer tensile 34×(2.5mm×8mm)	104.9 (53.7)*	2.50	205000	0.3
8	Fabric tape + External plastic sheath	109.9	5.50	215	0.3

*Mean radius used in Matlab code.**

Table 5-4: Engineering constants defining equivalent material properties of carcass and pressure armour.

Carcass				
Young`s modulus	Value (MPa)	Poison`s ratios	Shear modulus	Value (MPa)
$E_{longitudinal}$	100	$v_{12} = 0$	G_{S12}	3007
$E_{Circumferential}$	148173	$v_{13} = 0$	G_{S13}	3007
E_{radial}	148173	$v_{23} = 0$	G_{S23}	3007
Pressure armour				
Young`s modulus	Value (MPa)	Poison`s ratios	Shear modulus	Value (MPa)
$E_{longitudinal}$	100	$v_{12} = 0$	G_{S12}	59280
$E_{Circumferential}$	195408	$v_{13} = 0$	G_{S13}	59280
E_{radial}	195408	$v_{23} = 0$	G_{S23}	59280

Table 5-5: SI units used for Abaqus input data.

Quantity	SI units (mm)
Length	mm
Force	N
Mass	tonne (10^3 kg)
Time	s
Stress	MPa (N/mm^2)
Density	$tonne/mm^3$

5.3 Model 1 specific features

In model 1, the tensile armour is represented by linear two node beam elements (B32) and the rest of the layers are represented by linear 4 node shell elements with reduced integration (S4R). All layers are modelled with one element over thickness and meshed with the sweep technique. The cross section of model 1 is shown in **Figure 5-1**.

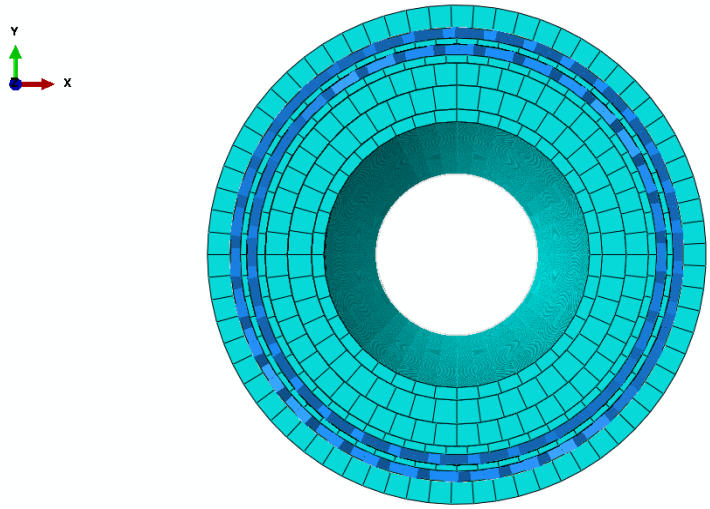

Figure 5-1: Cross section of model 1.

(i)

Non-metallic layers

The non-metallic layers represented by S4R elements are extruded based on inner radius. The thickness of these layers is defined in the edit section assignment dialogue box where the option offset from bottom is selected. The dimensions and material properties are shown in **Table 5-3**. The cylindrical parts are assigned material orientation with respect to a cylindrical coordinate system to get correct measurements of stress and displacement. The principal directions of the material orientation are shown in **Figure 5-2**.

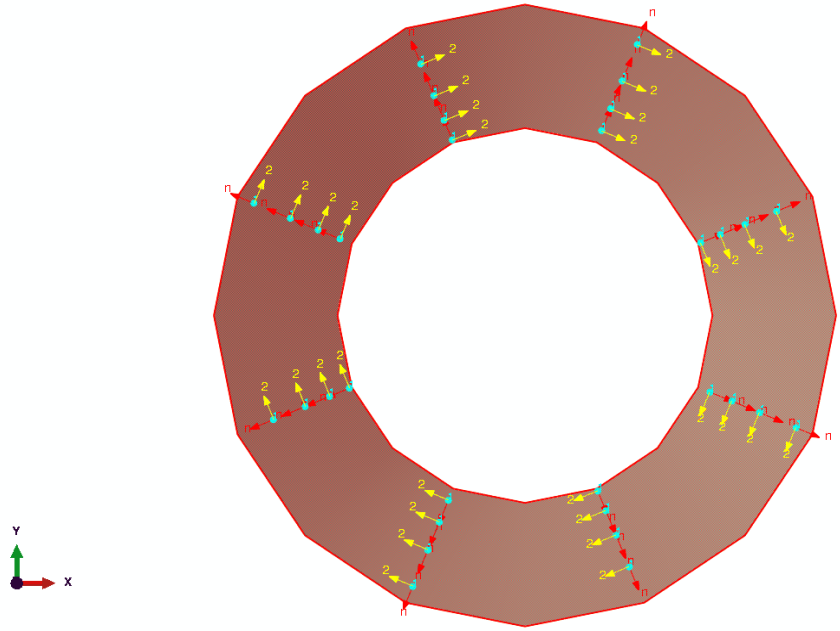

Figure 5-2: Material orientation assigned to cylindrical parts in model 1.

(ii)

Carcass and pressure armour

The carcass and pressure armour layers are modelled in a simplified manner by extruding cylinders of uniform wall thickness instead of the complex geometry of the interlocked profiles. These layers are also represented by S4R elements and the extrusion process is identical to the one for the non-metallic layers. The material orientation is also the same (see **Figure 5-2**). The aim is to attain the same stiffness for the simplified models as for the real layers. This is achieved by assigning an orthotropic material to the parts. The orthotropic materials are defined by engineering constants. That is Young`s modulus, shear modulus and Poison's coefficient in longitudinal, circumferential and radial direction. The Young`s modulus in the longitudinal direction is set to a very small value (100 MPa), as the axial stiffness of the carcass and pressure armour is negligible. The engineering constants used for the simplified layers are shown in **Table 5-4**.

(iii)

Tensile armour

The tensile armour wires are represented by B32 elements with cross section dimensions equal to the ones of the physical wires (8mm × 2.5mm). The procedure of creating the tensile armour layers is explained in following text.

In the create part dialogue box, the options 3D modelling space, part type deformable, and base feature point and coordinates are selected. Then, from the shape drop down menu, the wire and point to point option are selected. In the create wire feature dialogue box, spline is selected. By right clicking in the "points" field and choosing read from ASCII file, coordinates for the tensile wires are inserted in the dialogue box. The coordinates are generated with the Matlab codes presented in **Figure 5-3**.

```
clear all, close all
r=49.7; %Radiu of wire
L=1200; %length of wire
a=30; %lay angle
m=300; %coordinate number per pitch
P=2*pi*r/tan(a*pi/180); %pitch length
i=0; %no. of point

fileID = fopen('wire_inner_r_a_L_3xm.txt','w');

while(i<=m*L/P)
    x=r*cos(2*pi*i/m);
    y=r*sin(2*pi*i/m);
    z=i*P/m;
    i=i+1;
    fprintf(fileID,'%d,%d,%f\n',x,y,z);
end

fclose(fileID);
```

```
clear all, close all
r=53.7; %Radiu of wire
L=1200; %length of wire
a=30; %lay angle
m=300; %coordinate number per pitch
P=2*pi*r/tan(a*pi/180); %pitch length
i=0; %no. of point

fileID = fopen('wire_outer_r_a_L_3xm.txt','w');

while(i<=m*L/P)
    x=r*cos(-2*pi*i/m);
    y=r*sin(-2*pi*i/m);
    z=i*P/m;
    i=i+1;
    fprintf(fileID,'%d,%d,%f\n',x,y,z);
end

fclose(fileID);
```

Figure 5-3: Matlab code for generating wire coordinates.

As the wire made from point and coordinates contain no cross section, a rectangular beam profile is created with the dimensions 8mm × 2.5mm. A material with properties of carbon steel is also created, which, in addition to the beam profile, is assigned to the helical wire. Beam section orientation is also assigned to the wire, where the direction 1 is in the lay direction of the wire and the normal direction is pointing away from the centre of helix as shown in **Figure 5-4**.

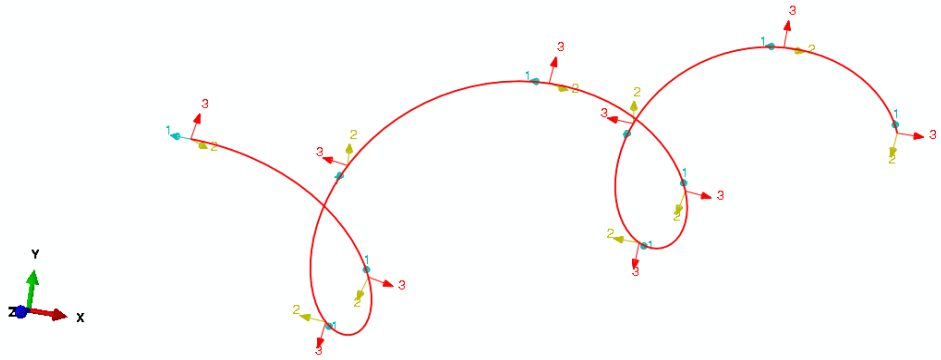

Figure 5-4: Single wire with beam orientation in model 1.

In the assembly module, an instance is created from the wire (part) and multiplied with radial pattern according to the number of wires in the respective layers. The total angle is set to 360 degrees and the radial pattern is created with respect to the longitudinal axis of the pipe.

The beam elements have no nodes in corners or on edges, but one node in the cross section centre at each end. As a result, the wires cannot be cut at an angle to coincide with the ends of the other layers. However, the end nodes do coincide with the ends of the other layers. Moreover, the mesh is only visible on the wire inside the rectangular profile. Both of these effects are shown in **Figure 5-1** and **Figure 5-5**.

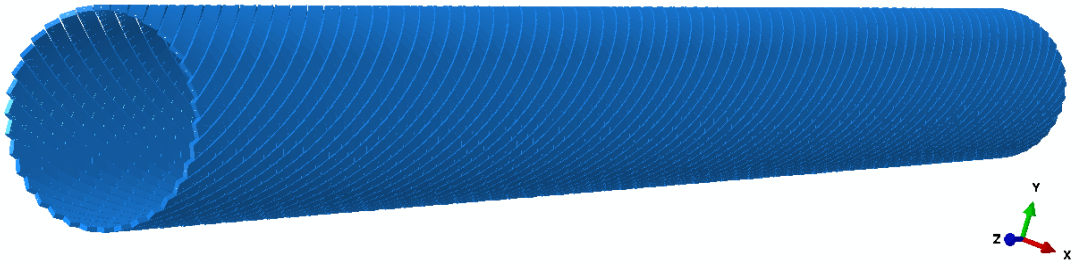

Figure 5-5: Outer layer of tensile armour meshed with beam elements in model 1.

5.4 Model 2 specific features

The cylindrical layers in model 2 are represented by linear 4 node shell elements (S4R) and the tensile wires are represented by linear 8 node hexahedral elements (C3D8R). All cylindrical layers are modelled with one element over thickness and all layers are meshed with the sweep technique. The cross section of model 2 is shown in **Figure 5-6**.

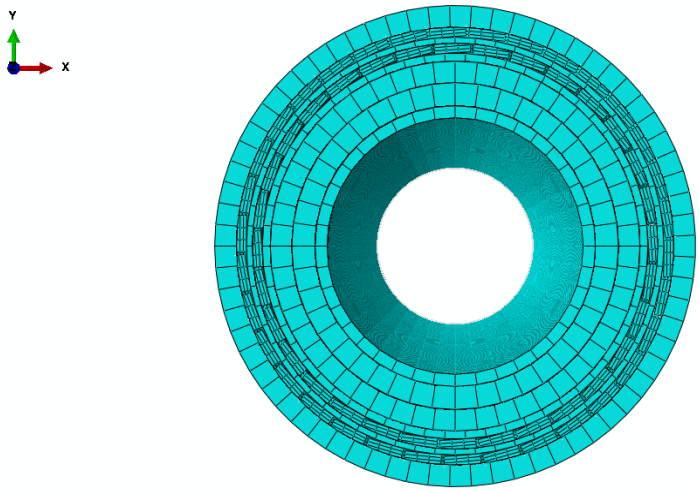

Figure 5-6: Cross section of FE model 2.

(i)

Cylindrical layers

Metallic and non-metallic cylindrical layers in model 2 are identical to the cylindrical layers in model 1. Because of this, the modelling procedure for these layers is not repeated as it would be a meaningless duplication. However, the process of modelling the tensile armour layers is explained next.

(ii)

Tensile armour

The tensile wires are represented by C3D8R elements and revolved from a sketch of the tendon cross section (2.5mm x 8mm). The cross section centre is located at a distance equal to the mean radius of the layer from the centre of sketch grid.

In the revolve dialogue window, the move sketch normal to path option is selected and the wire cross section is revolved based on an angle and pitch. The pitch of the outer tensile wire which is 598 mm is used for both inner and outer wires. However, the actual pitch of the inner tensile armour is 554.5 mm. The angle is increased so the helix length exceeds two pitches of the outer tensile armour. This is done because the wire ends need to be cut at an angle to coincide with the ends of the other layers.

In the part module, a datum plane is introduced just within wire end 1 and normal to pipe axis. Partition cell is created from said datum plane and the small piece of wire is removed. A new datum plane is offset from the first plane by 1200mm and the same procedure is done to cut end 2. Now, the wire ends should coincide with the ends of the other layers and the distance between wire ends is 1200 mm.

As the ends of the wire no longer are perpendicular to the lay direction, the element edges across the wire will not be either. To measure axial stress in the wire, element edges across wire must be perpendicular. This is achieved by introducing a partition sufficiently close to each wire end.

At end 1, a datum plane is offset a couple of centimetres from the datum plane introduced previously. Then, a new datum plane is rotated from the last datum plane. Partition edge is created with the rotated datum plane. This creates a point on the wire edge. Next, partition cell is created with the option, define cutting plane from point and normal. The point created from partition edge is selected. The cell-partition divisions the wire perpendicular to the lay direction. To repeat the partition at the opposite end, a datum plane is offset from the rotated datum plane and located in the proximity of end 2. The partition edge and cell procedure is repeated. One wire with datum planes is shown in **Figure 5-7**. After meshing, the element edges across wire are perpendicular to the lay direction between the two partitions, yielding correct axial stress measurements.

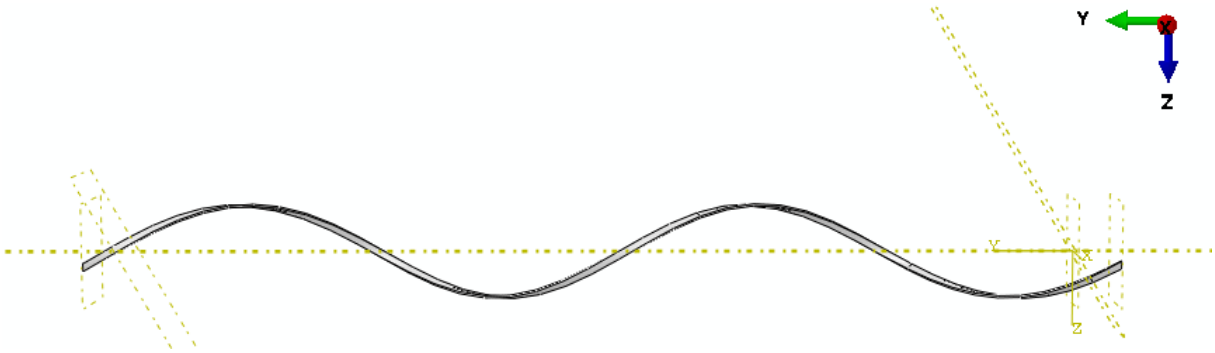

Figure 5-7: Tensile wire with datum planes in model 2.

Material orientation is assigned to the part in order to get correct measurements of stress and displacement. The orientation is defined with the discrete option. Direction 1 is selected for the primary axis and defined along one wire edge. Normal axis is set to direction 3 and defined as normal to the inner wire surface. The principal directions of the material orientation are shown in **Figure 5-8**.

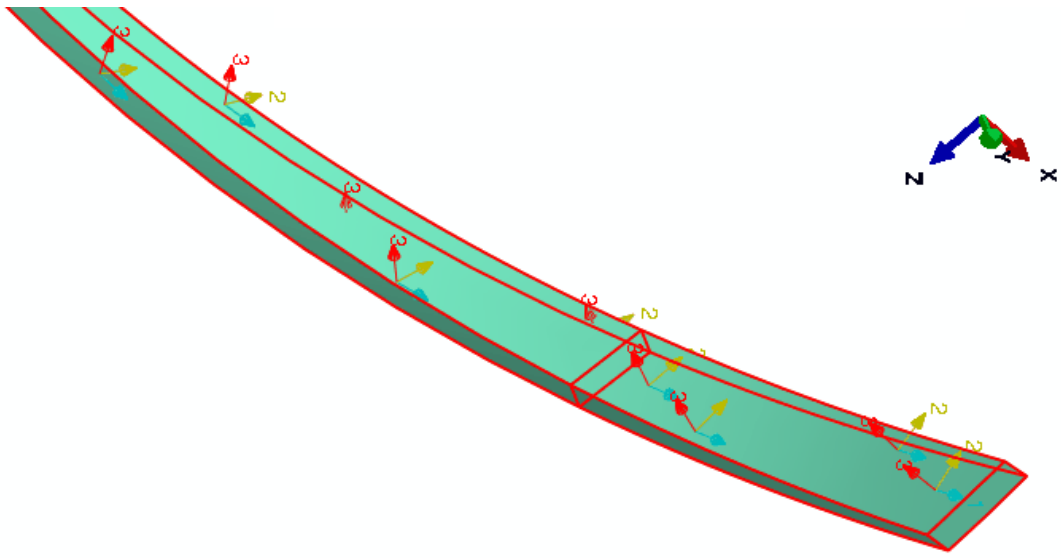

Figure 5-8: Material orientation assigned to tensile wires in model 2.

In the assembly module, an instance is created from the wire part and multiplied with radial pattern according to the number of wires in the respective layers. The total angle is set to 360 degrees and the radial pattern is created with respect to the pipe longitudinal axis. As shown in **Figure 5-9**, the element edges are perpendicular to the lay direction after the third element from the wire ends.

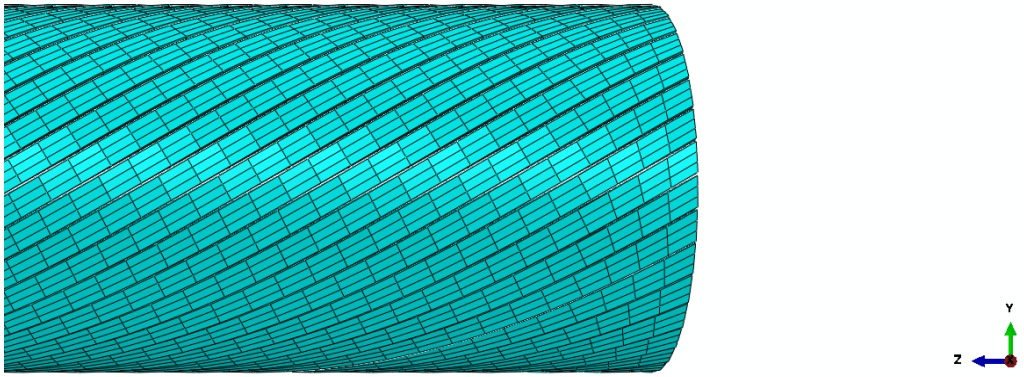

Figure 5-9: Tensile armour with partition meshed in model 2.

5.5 Model 3 specific features

All layers in model 3 are represented by linear hexahedral 8 node solid elements (C3D8R) and the medial axis algorithm is used during meshing to get one element over thickness in the cylindrical layers. The sweep technique is used to mesh all layers. Because the tensile wires are modelled in the same manner as in model 2, the process is not repeated. The cross section of model 3 is shown in **Figure 5-10**.

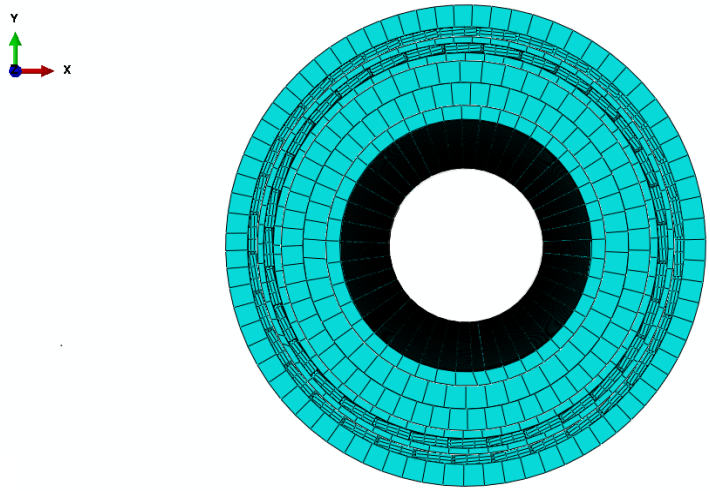

Figure 5-10: Cross section of FE model 3.

(i)

Non-metallic layers

The non-metallic layers are extruded based on a sketch of the inner and outer radius of each layer. The material properties and dimensions are found in **Table 5-3**. The cylindrical layers are assigned material orientation with respect to a cylindrical coordinate system to get correct measurements of stress and displacement. Direction 1 is in the radial, direction 2 is in the circumferential and direction 3 is in the longitudinal direction, respectively. The principal directions are shown in **Figure 5-11**.

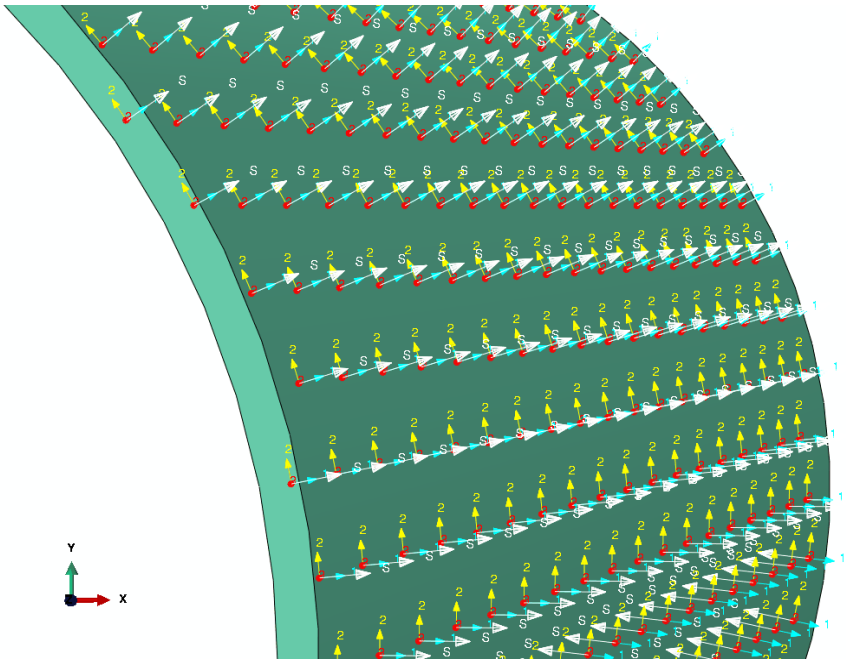

Figure 5-11: Material orientation assigned to cylindrical parts in model 3.

(ii)

Carcass and pressure armour

The carcass and pressure armour are modelled in a simplified manner by extruding a cylinder of uniform wall thickness instead of the complex geometry of the interlocked profiles. Because these layers are also represented by C3D8R elements, the extrusion process is identical to the one for non-metallic layers. The material orientation is also the same (see **Figure 5-11**). The aim is to attain the same stiffness for the simplified models as for the real carcass and pressure armour layers. This is achieved by assigning orthotropic materials to these parts. The orthotropic materials are defined by engineering constants: namely, Young`s modulus, shear modulus and Poison's coefficient in longitudinal, circumferential and radial direction. The Young`s modulus in the longitudinal direction is set to a very small value (100 MPa), as the axial stiffness of the carcass and pressure armour is negligible. The engineering constants used for the simplified layers are shown in **Table 5-4**.

5.6 Wire and edge numbering

At point a in **Figure 5-12**, the wire number 1 of the inner and outer tensile layers is marked with a red ellipse. The wires are numbered in the counter-clockwise direction from this point when looking at the riser model in the global xy-plane. The letters i and o are included when referring to a specific wire to distinguish between the outer and inner layer. The inner and outer wire at point a are referred to as wire-i-1 and wire-o-1, respectively. This notation is used to identify wires in the analyses. Point b in the same figure illustrates the convention used for numbering the wire edges and applies to both layers.

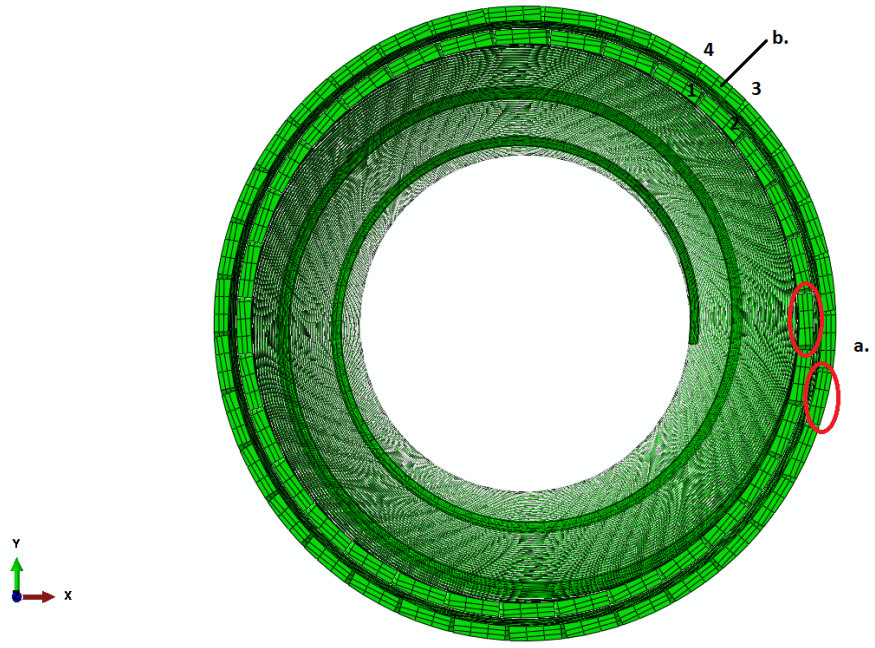

Figure 5-12: Two layers of tensile armour with wire number 1 at point a, and edge numbers at point b.

5.7 Boundary conditions and loads

The different layers are free to slide against each other, but at both ends all the nodes are constrained to a reference point in the centre of the cross section to simulate perfect end fittings. Kinematic coupling is used for the constraints. Boundary conditions and loads are imposed on the reference point at each end. Boundary conditions are introduced in the initial step and loads in step one.

(i)

Tension

The first load case is tension and the boundary conditions are as follows:

Initial condition:

- At end 1: Fixed rotation and translation in all directions.
- At end 2: Fixed rotation in all directions and fixed translation in x and y direction. The pipe is free to move along the longitudinal axis.

Loading case 1:

- At end 2: The pipe is gradually tensioned until a maximum load of 250kN is reached.

(ii)

Bending

The second load is bending. The transverse bending load could be applied directly, but it would be a great computational effort. Therefore, end rotations are applied instead.
Initial condition:

- At end 1: Fixed rotation in y and z direction. Fixed translation in all directions.
- At end 2: Fixed rotation in y and z direction. Fixed translation in y and x direction. The pipe is free to move in the longitudinal direction.

Loading case 2:

- At end 1: A positive rotation angle about x axis is gradually increased until the maximum rotation of 0.06 radians is reached.
- At end 2: A negative rotation angle about x axis is gradually increased until the maximum rotation of 0.06 radians is reached.

5.8 Contact

Contact is accounted for by the general contact algorithm in Abaqus/Standard which primarily uses the finite-sliding, surface-to-surface contact formulation. Surface-to-edge and edge-to-edge are used as supplementary formulations. The contact domain contains selected surface pairs. Choosing this option instead of "included surface pairs: all" reduces computational time and prevent complications which may occur when the contact algorithm consider surfaces which do not interact with each other.

(i)

Contact properties

Surface interactions in terms of normal and tangential behaviour is considered during simulations. Two contact property models are used to define the surface interactions, the first during the initial step and the second during step one of the simulation. In the initial step, the normal behaviour is accounted for with hard contact which is the default contact pressure-overclosure relationship in Abaqus. The following conditions are provided with hard contact:

- Contact pressure is not transmitted between the surfaces except when slave nodes are in contact with the master surface.
- Penetration is prohibited at each constraint point.
- The magnitude of contact pressure transmitted is unlimited when the surfaces are in contact.

The penalty method is used to enforce the contact constraints for normal behaviour. This is the default constraint enforcement method for hard contact and it is a stiff approximation of

hard contact, which means that the condition of no penetration is approximately satisfied. The tangential behaviour is defined with a frictionless formulation during the initial step to allow nodal adjustments during analysis pre-processing (more on this in (ii) Initial contact control).

During step one, the normal behaviour is governed by hard contact as in the initial step. The tangential behaviour is now including friction and the penalty method is selected for the friction formulation with isotropic directionality. A friction coefficient of 0.15 is used in the analyses.

(ii)

Initial contact control

Nodes may be initially penetrating adjacent surfaces as a result of small mismatches caused by the mesh generating process. For small overclosures, the general contact algorithm positions these nodes at the surface by default with strain free adjustments during pre-processing. Running simulations of pure axial loading with the default contact initialization method yields bending stress in the tensile wires. This indicates that there is something profoundly wrong with the FE model. Changing the contact initialization method to treat as interference fits and let Abaqus ignore initial overclosures and openings greater than 0.8 millimetres solves this problem. The Abaqus users guide recommend that friction interactions are introduced after the initial interference fits are resolved as the presence of a friction model may compromise the resolve [18]. This is why two contact property models are used in the simulations.

5.9 Solution method

The solution is found with the full Newton-Raphson method. Shear locking is taken into account by using reduced integration elements. When analysing the flexible riser models with the static procedure, the incremental solution tends to diverge. Using the asymmetric equation solver in dynamic implicit procedure and choosing quasi-static application in the edit step dialog box improves convergence of the simulations. This is because the inertia effects introduced in this procedure regularize unstable behaviour. Time increments are automatically adjusted for nonlinear dynamic procedures in Abaqus. For quasi-static applications, the size of the increment is reduced if convergence is slow or the increment seems to be diverging. If previous increments have high convergence rates, then the increment size is increased quite aggressively.

6 Material Validation and Convergence

Before performing the analyses, it is necessary to confirm that the simplified geometry and equivalent properties are reasonable. Furthermore, it would be wise to investigate element sizes and find the minimum size needed to yield good results to avoid unnecessary long computations.

6.1 Evaluation of equivalent properties

The equivalent properties from approach 1 are used in the carcass and pressure armour layers. These values are evaluated by simulating an internal pressure load case for both shell and solid model and comparing the hoop stress results from simulations (S22) to analytical values as discussed in section 4.3.

Element size 5 is used in both models. The internal pressure is set to 20 MPa both in the FE analyses and in the analytical equations. External pressure is assumed to be 0 MPa in the analytical calculations as atmospheric pressure would be present at both the inside and the outside of the pipe wall. The engineering constants which define the equivalent material properties are shown in the modelling section 5.2. All the hoop stress simulations are performed with the following boundary conditions: fixed translational and rotational DOFs at end 1. At end 2, free to move in the longitudinal direction, but all other DOFs are fixed. This allows pipe contraction in longitudinal direction when the pipe expand radially due to the applied internal pressure. The results of the simulations are with respect to the cylindrical coordinate system used to define material orientations.

(i)

Analytical hoop stress

The analytical values of hoop stress are calculated with Lamé`s equations. Data used in the calculations are found in **Table 6-1**, where dimensions a, and b are the inner and outer radii of the respective layers, calculated according to approach 1.

Table 6-1: Data for analytical equations, equivalent properties approach 1.

Layer	a (mm)	b (mm)	P_i (MPa)	P_o (MPa)
Carcass	32.1789	35.25	20	0
Pres. armour	41.0499	46.45	20	0

Hoop stress at the inner wall of the carcass layer:

$$\sigma_{\theta\theta}(r=a) = 20\frac{32.1789^2}{35.25^2 - 32.1789^2}\left(1 + \frac{35.25^2}{32.1789^2}\right) = 220.015\ MPa$$

Hoop stress at the inner wall of the pressure armour layer:

$$\sigma_{\theta\theta}(r=a) = 20\frac{41.0499^2}{46.45^2 - 41.0499^2}\left(1 + \frac{46.45^2}{41.0499^2}\right) = 162.651\ MPa$$

(ii)

Hoop stress in model 2

As shown in **Figure 6-1**, the hoop stress (S22) measured mid-pipe at the internal carcass wall in model 2 is found to be 209 MPa, which is about 5% less than the value found from analytical equations.

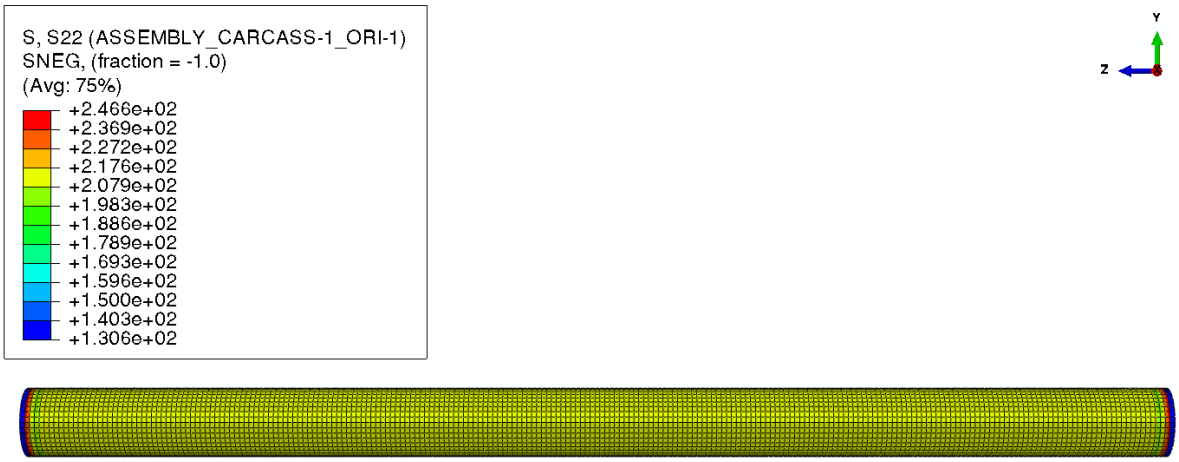

Figure 6-1: Hoop stress (S22) at internal carcass wall in model 2.

As shown in **Figure 6-2**, the hoop stress (S22) measured mid-pipe at the internal pressure armour wall in model 2 is found to be 152 MPa, which is about 6.5% less than the value found with analytical equations.

Figure 6-2: Hoop stress (S22) at internal pressure armour wall in model 2.

(iii)

Hoop stress in model 3

As shown in **Figure 6-3**, the hoop stress (S22) measured mid-pipe at the internal carcass wall in model 3 is found to be 216 MPa, which is about 2% less than the analytical value.

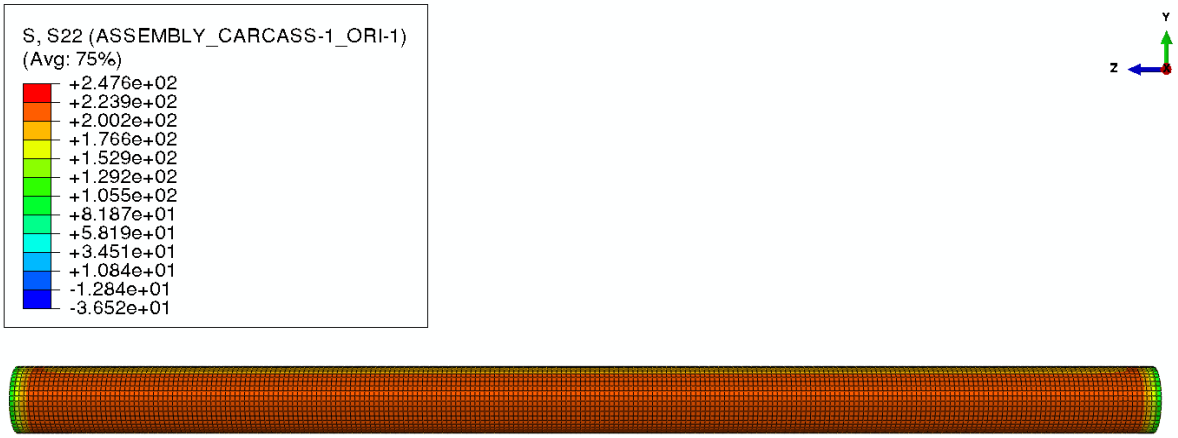

Figure 6-3: Hoop stress (S22) at internal carcass wall in model 3.

As shown in **Figure 6-4**, the hoop stress (S22) measured mid-pipe at the internal wall is found to be 152 MPa, which is about 6.5% less than the analytical value.

Figure 6-4: Hoop stress (S22) at internal pressure armour wall in model 3.

(iv)

Summary

The analytical and numerical results are presented in **Table 6-2**. The numerical hoop stress values from the four simulations deviate no more than 6.5% from the analytical values. Furthermore, the numerical values are smaller than the analytical ones, which is reasonable as analytical calculations are more conservative in nature. The equivalent material properties

should therefore be suitable to represent the material in the simplified models of carcass and pressure armour during stress analyses.

Table 6-2: Hoop stress values from simulations and analytical equations.

Layers	Analytical MPa	Shell MPa	Deviation	Solid MPa	Deviation
Carcass	220.015	209	5%	216	2%
Pressure armour	162.651	152	6.5%	152	6.5%

6.2 Convergence study

As discussed in previous sections, the number of elements and degrees of freedom of the model will have a large impact on the computational time during analysis. Therefore, a convergence study is performed to find the element size which yields good results while the computational effort is kept at a minimum. Two parameters are considered in the study: The global seeds, in all layers, which determines the approximate element size (keep in mind that all cylindrical layers have one element over thickness), and the edge seeds on wire ends which defines the number of elements over tensile wire cross section. The convergence study is performed on the shell model as the simulation take less time compared to the solid model.

An axial load of 250 kN is applied to the reference point at end 2 and the axial wire stress (S11) is measured mid-pipe in a single wire for both inner and outer tensile armour layer in addition to the longitudinal deformation (U3) of the riser. Axial stress is evenly distributed between wires in the respective layers, thus wire-i-1 and wire-o-1 are arbitrary selected for measurements. For the different combinations of element sizes, the number of elements and nodes defined by user in addition to total number of variables in the model are presented together with the results.

(i)

Global seeds

The wire cross section consists of nine elements during the study of global seeds. A simulation with global element size five for all layers is performed first. The results from this simulation are used as a reference for the following simulations with larger elements. After adjusting the element size in the cylindrical parts to ten and keeping the element size five for wires, S11 remains unchanged and U3 is increased by less than 0.004% (see **Table 6-3**). Adjusting the element size to ten for the wires as well yields about the same results for S11, but U3 increases by about 27% which is not reasonable. Difference in element size between wires and cylindrical layers could yield good results for larger elements, however, adjusting the size to twelve and fifteen yields about 36% increase of U3. The largest global element size yielding good results is the combination of size ten for cylindrical parts and five for wires.

Table 6-3: Mesh information for different element sizes and corresponding global U3 and S11 in wire due to tension.

Element size		No. of elements	No. of nodes	No. of variables	U3 Global mm	S11 wire MPa	
Cylinders	Wires					Inner	Outer
5	5	242852	372253	3838389	1.887	228	199
10	5	159692	224413	2507829	1.894	228	199
10	10	101137	165695	1625103	2.584	229	195
12	15	68423	112136	1106898	2.940	222	199

(ii)

Edge seeds

The global element size is set to ten for cylinders and five for wires during the study of edge seeds. Results from the simulation with element size ten for cylinders and size five for wires with nine elements over wire cross section are used as reference for the following simulations. Starting with one element over wire cross section, U3 is found to be about 43% larger and S11 in the inner wire is found to be about 19% larger than the reference values (see **Table 6-4**) which is not reasonable. Adjusting the number of elements to four over cross section, U3 is still more than 28% larger and S11 is about 10% larger than the reference values.

Table 6-4: Mesh information for different no. of edge seeds and corresponding global U3 and S11 in wire due to tension.

No. of elements over		No. of elements	No. of nodes	No. of variables	U3 Global mm	S11 wire MPa	
Thickness	Width					Inner	outer
1	1	87308	115045	1731165	3.351	280	183
2	2	114452	160615	2091759	2.639	253	180
3	3	159692	224413	2507829	1.894	228	199

(iii)

Summary

It is found from the simulation above that global element size ten for cylinders and size five for wires with nine elements over wire cross section is the mesh with smallest number of elements that yields good results. One simulation with the same combination of global seeds and edge seeds is done for model 3 to verify this mesh for the solid model. U3 is found to be 1.963 mm which is 3.5% more than for model 2. S11 in the inner wire is found to be 231 MPa and S11 in the outer wire is found to be 199 MPa which is 1.3% more and the same value as for model 2, respectively. For model 3, this mesh has 165942 elements, 315488 nodes and 2694108 variables. The results are reasonable, therefore this mesh is used in simulations for both models from this point.

7 Analyses Results and Discussion

Stress analyses are performed for the intact riser and with damaged tensile wires. Two wires are ruptured in the damaged case. The load scenarios are pure tension and bending. The stress analyses are performed with the boundary conditions and loads described in section 5.7.

7.1 Intact wires

It is important that the FE models replicate the behaviour of the physical pipe for the analyses results to be considered as having any significant value and for the models to be suited for integrity assessment of flexible risers with or without damaged tensile armour. The models are verified by comparing the axial stiffness to the one measured in the physical pipe during experimental tests in the study by De Sosa [13]. The bending stiffness is evaluated by comparing the axial stress in wires due to bending to calculated analytical values.

(i)

Tension

Axial stiffness of the models can be calculated by dividing the applied tensile force by the elongation caused by said loading. The length of the FE models is 1200mm, and a tensile load of 250 kN is applied at end 2 of each model. Axial stiffness measured on the physical pipe in De Sosa`s study is 153000 kN. Deformation due to axial load and calculated axial stiffness of the FE models are presented below.

Model 2

The longitudinal displacement of model 2 is 1.894 mm, yielding axial stiffness $EA = \frac{250\ kN}{\left(\frac{1.894mm}{1200mm}\right)} = 158395\ kN$. This is about 3.4% more than the axial stiffness of the physical riser.

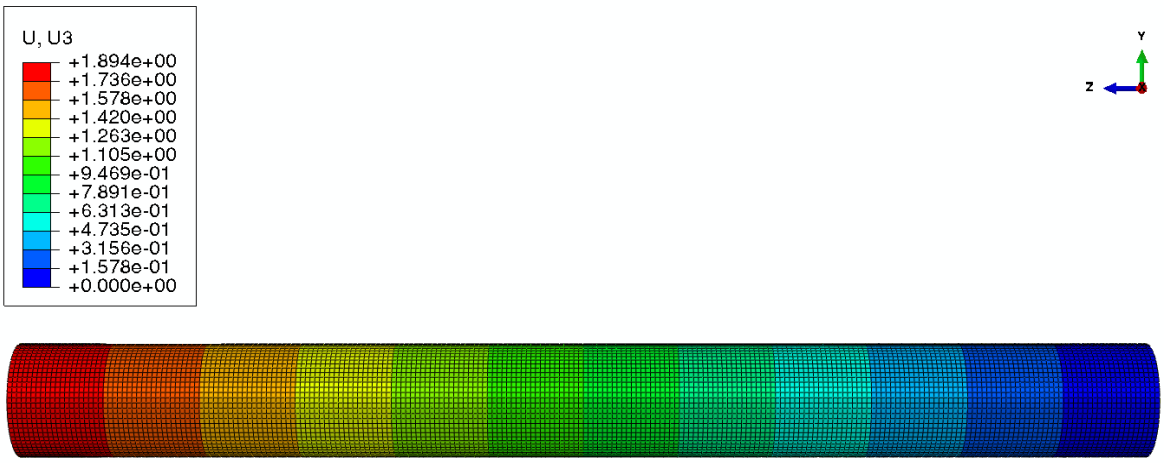

Figure 7-1: Longitudinal deformation (U3) of model 2 due to tensile load of 250 kN.

Model 3

The longitudinal displacement of model 3 is 1.963 mm, yielding axial stiffness $EA = \frac{250kN}{1.963/1200} = 152827\ kN$ which is 0.001% less than the axial stiffness of the physical riser.

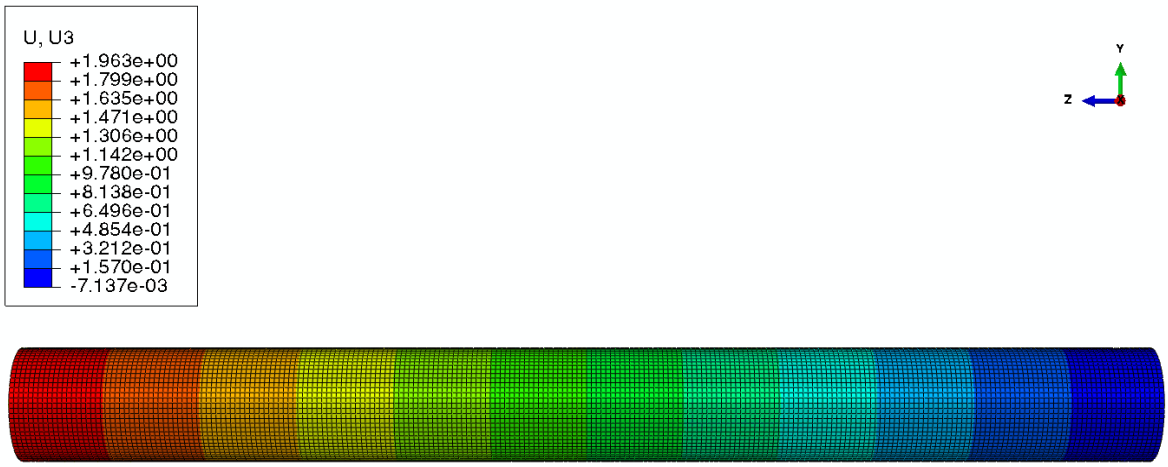

Figure 7-2: Longitudinal deformation (U3) of model 3 due to tensile load of 250 kN.

(ii)

Bending

The actual bending stiffness of the physical pipe is not given or calculated in [13]. Therefore, the models are evaluated by comparing axial stress in wires due to bending to analytical values calculated with equations from section 2.2. As discussed in section 2.2, the wire path during bending will be somewhere between the two limits, the geodesic and loxodromic path. Thus, the axial stress amplitudes measured in the simulations should be within the analytical amplitude range. During simulations, a rotation of 0.06 radians is imposed on the reference point at both ends to bend the pipe. This rotation corresponds to a curvature of approximately 0.1 m^{-1} which is used in the analytical calculations. End effects are avoided by only considering the pipe section between 299 mm and 897 mm from end 1 which corresponds to the pipe section from half a pitch to one and a half pitch of the outer tensile layer.

Analytical values

The equations from section 2.2 are modified to plot the stress over pipe distance instead of angular coordinates. The analytical axial stress due to pipe curvature is plotted in Matlab. Assuming the wire undertake the geodesic path (no friction), analytical dynamic axial wire stress due to normal curvature is found with eq. 2.4. As shown in **Figure 7-3**, the peak values should occur about 450 mm and 750 mm from end 1. This corresponds to the angular coordinates 2π and 3π. The axial stress due to bi-normal curvature ($\Delta\sigma_{11}^{M3}$) is zero for the geodesic assumption.

$$\Delta\sigma_{11}^{M_2} = \frac{3}{2}\cos^2\frac{\pi}{6}\cdot 0.1\ m^{-1}\cdot 0.0025m\cdot 205000\ MPa\cdot\cos 2\pi = 57.7\ MPa$$

$$\Delta\sigma_{11}^{M_3} = 0$$

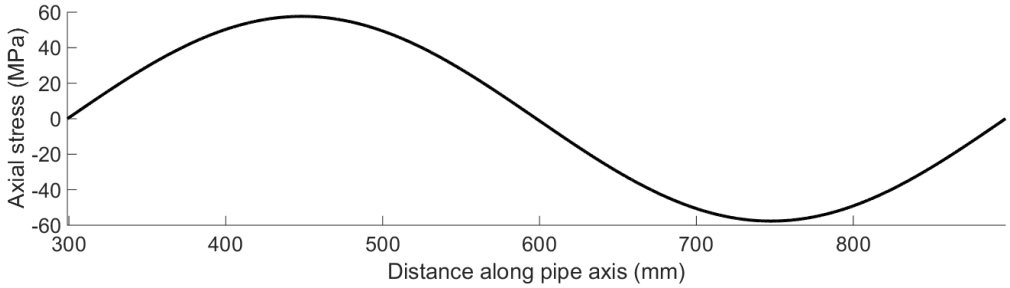

Figure 7-3: Dynamic axial wire stress due to normal curvature ($\Delta\sigma_{11}^{M2}$) assuming the geodesic path.

Assuming the loxodromic path (infinite friction), analytical dynamic axial wire stress due to normal curvature is found with eq. 2.7. As shown in **Figure 7-4**, the peak values should occur about 450 mm and 750 mm from end 1, which in angular coordinates, is 2π and 3π.

$$\Delta\sigma_{11}^{M_2} = \frac{1}{2}\cos^4\frac{\pi}{6}\cdot 0.1\ m^{-1}\cdot 0.0025\ m\cdot 205000\ MPa\cdot\cos 2\pi = 14.4\ MPa$$

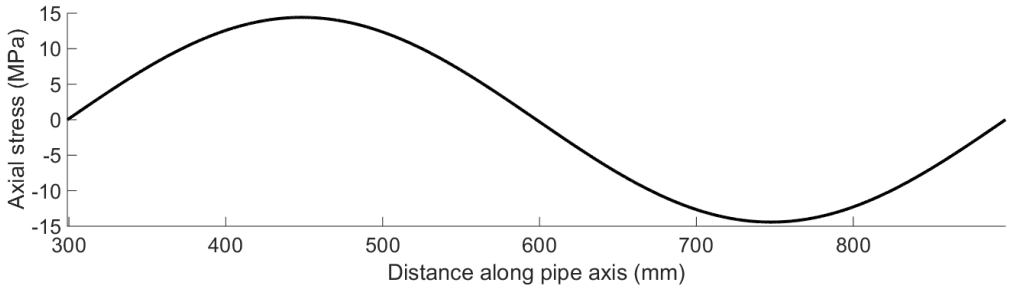

Figure 7-4: Dynamic axial wire stress due to normal curvature ($\Delta\sigma_{11}^{M2}$) assuming the loxodromic path.

Assuming the loxodromic path, analytical axial wire stress due to bi-normal curvature is found with eq. 2.8. As shown in **Figure 7-5**, the peak values should occur about 300 mm, 600 mm and 900 mm from end 1. In angular coordinates, this equals to 3π/2, 5π/2 and 7π/2.

$$\Delta\sigma_{11}^{M_3} = \frac{1}{2}\cos\frac{\pi}{6}\cdot(1+\sin^2\frac{\pi}{6})\cdot 0.1\ m^{-1}\cdot 0.008\ m\cdot 205000\ MPa\cdot\sin\frac{5\pi}{2} = 88.8\ MPa$$

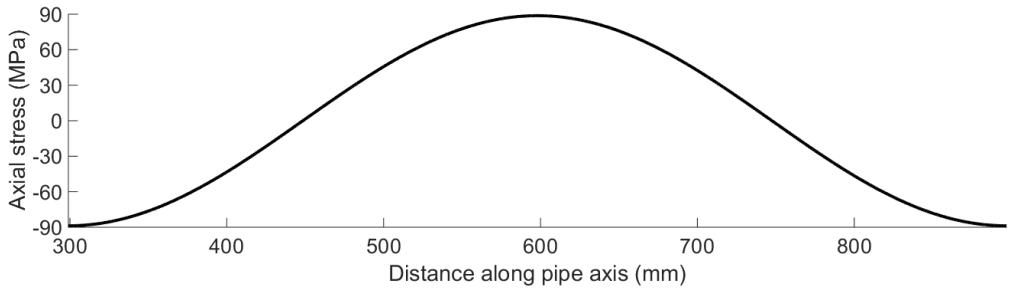

Figure 7-5: Dynamic axial wire stress due to bi-normal curvature ($\Delta\sigma_{11}^{M3}$) assuming the loxodromic path.

S11 measurements

One wire at the tensile and compressive side of the riser in the inner and outer tensile layer is considered for each FE model and the axial stress (S11) is measured along the four edges of the wires because the magnitude of stress is largest here. The wire whose cross section is located closest to the global y axis at the compressive and tensile side mid-pipe is selected for measurement in both layers. The wire edges are numbered according to the convention in **Figure 5-12**. A path is created along each wire edge and the XY data is exported as a .txt file. The XY data is used to calculate and plot the dynamic stress due to normal wire curvature ($\Delta\sigma_{11}^{M2}$) and bi-normal wire curvature ($\Delta\sigma_{11}^{M3}$). $\Delta\sigma_{11}^{M2}$ has its maximum values at the outer and inner wire surfaces and $\Delta\sigma_{11}^{M3}$ has its maximum values at the wire side surfaces. Stress ranges of the wire surfaces are defined in **Table 7-1** where subscript 1-4 denotes the edge number.

Table 7-1: Definition of stress ranges on wire surfaces.

Surface	Δσ (MPa)
Inner (i)	$S11_1 - S11_2$
Outer (o)	$S11_3 - S11_4$
Left (l)	$S11_4 - S11_1$
Right (r)	$S11_2 - S11_3$

Model 2

For the inner armour layer, wire-i-9 is selected at the compressive side and wire-i-25 at the tensile side. The axial stress distribution (S11) along the edges of wire-i-9 is shown in **Figure 7-7**. The stress along edges is symmetric about the value -2.4 MPa. The dynamic surfaces stresses ($\Delta\sigma_{11}$) are shown in **Figure 7-6** and **Figure 7-8**. The peak values are shown in **Table 7-2** and **Table 7-3**.

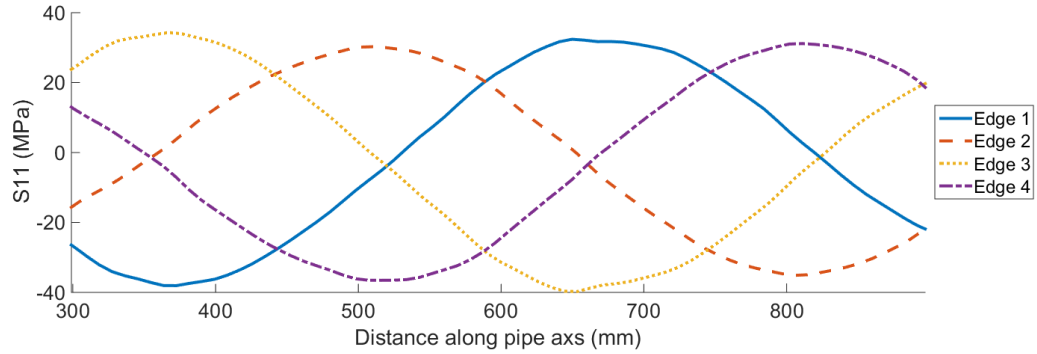

Figure 7-7: S11 along edges of wire-i-9 in model 2.

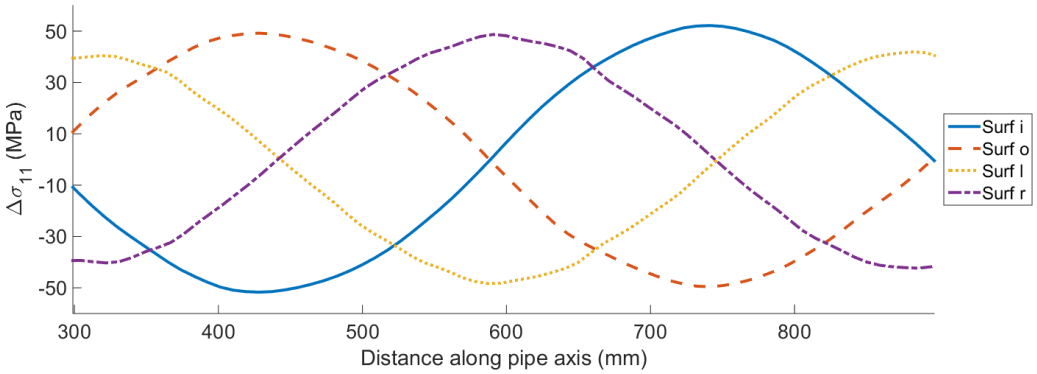

Figure 7-6: $\Delta\sigma_{11}$ along surfaces of wire-i-9 in model 2.

Table 7-2: Dynamic stress peaks in wire-i-9 in model 2.

	$\Delta\sigma_{11}^{M2}$		$\Delta\sigma_{11}^{M3}$	
Position mm	Inner surf.	Outer surf.	Left surf.	Right surf.
300	-	-	39.5	-39.3
450	-51.5	48.9	-	-
600	-	-	-48.2	48.2
750	51.9	-49.1	-	-
900	-	-	41.6	-41.8

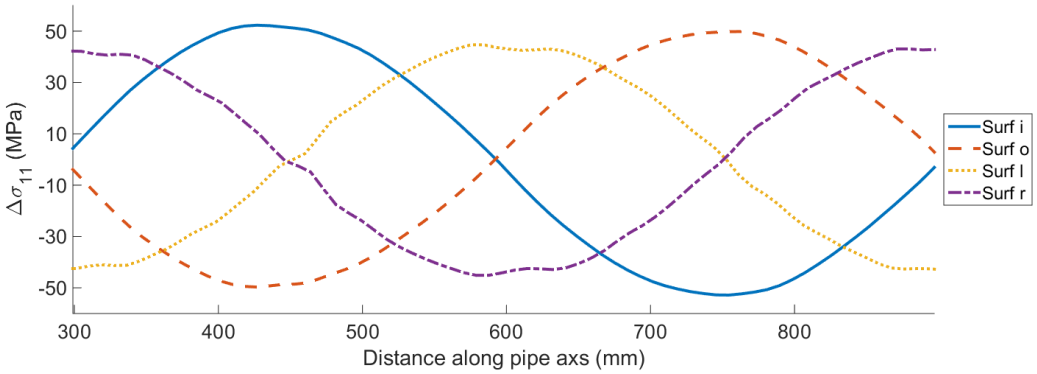

Figure 7-8: $\Delta\sigma_{11}$ along surfaces of wire-i-25 in model 2.

Table 7-3: Dynamic stress peaks in wire-i-25 in model 2.

	$\Delta\sigma_{11}^{M2}$		$\Delta\sigma_{11}^{M3}$	
Position mm	Inner surf.	Outer surf.	Left surf.	Right surf.
300	-	-	-42.5	42.2
450	51.2	-48.5	-	-
600	-	-	41.1	-40.5
750	-52.8	49.6	-	-
900	-	-	-43.0	43.4

For the outer armour layer, wire-o-10 is selected for the compressive side and wire-o-28 for the tensile side. The dynamic surfaces stresses ($\Delta\sigma_{11}$) are shown in **Figure 7-9** and **Figure 7-10**. The peak values are shown in **Table 7-4** and **Table 7-5**.

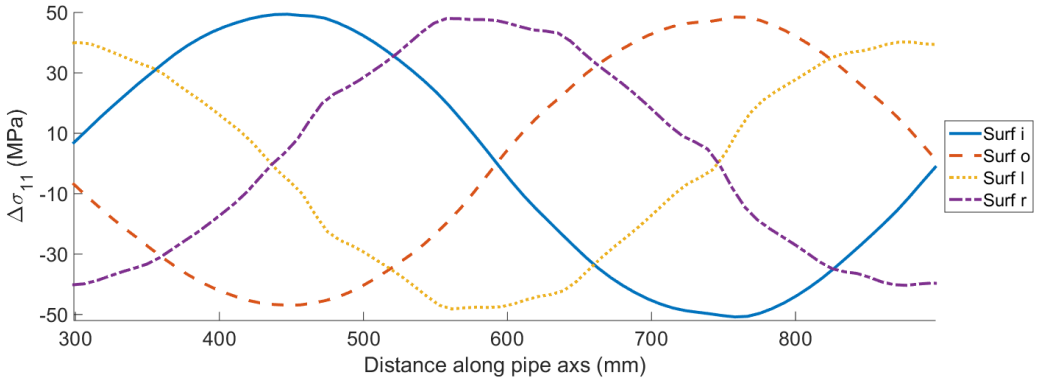

Figure 7-9: $\Delta\sigma_{11}$ along surfaces of wire-o-10 in model 2.

Table 7-4: Dynamic stress peaks in wire-o-10 in model 2.

	$\Delta\sigma_{11}^{M2}$		$\Delta\sigma_{11}^{M3}$	
Position mm	Inner surf.	Outer surf.	Left surf.	Right surf.
300	-	-	40.1	-40.2
450	49.4	-46.9	-	-
600	-	-	-46.5	46.4
750	-50.4	47.7	-	-
900	-	-	39.6	-39.8

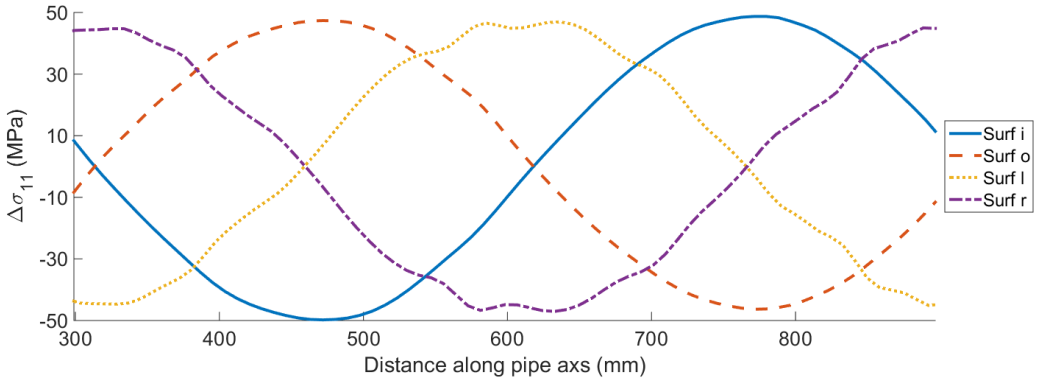

Figure 7-10: $\Delta\sigma_{11}$ along surfaces of wire-o-28 in model 2.

Table 7-5: Dynamic stress peaks in wire-o-28 in model 2.

	$\Delta\sigma_{11}^{M2}$		$\Delta\sigma_{11}^{M3}$	
Position mm	Inner surf.	Outer surf.	Left surf.	Right surf.
300	-	-	-44.3	44.2
450	-48.4	45.9	-	-
600	-	-	44.9	-44.8
750	47.8	-45.3	-	-
900	-	-	-44.6	44.8

As shown in **Figure 7-6** to **Figure 7-10**, the peak values of $\Delta\sigma_{11}^{M2}$ and $\Delta\sigma_{11}^{M3}$ occur at approximately the same locations as the analytical equations predict. The dynamic stress due to normal curvature in both inner and outer wire are between the values calculated with geodesic and loxodromic assumption and closest to the geodesic. This could be due to the small curvature. For larger curvature, the slip force would increase to overcome the friction force, resulting in increased axial stress. The dynamic stress due to bi-normal curvature is about mid-range between the two limits. Furthermore, the S11-data for wire-i-9 is slightly skewed to the negative. This skewedness could be the result of Abaqus taking friction into account during simulations, which the analytical methods do not.

Model 3

The same wires are selected in model 3 as in model 2. The axial stress distribution (S11) along the edges of wire-i-9 is shown in **Figure 7-12**. The plot is symmetric about approximately -2.3 MPa. The dynamic surface stresses ($\Delta\sigma_{11}$) in wire-i-9 and wire-i-25 are shown in **Figure 7-11** and **Figure 7-13**. The peak values are shown in **Table 7-6** and **Table 7-7**.

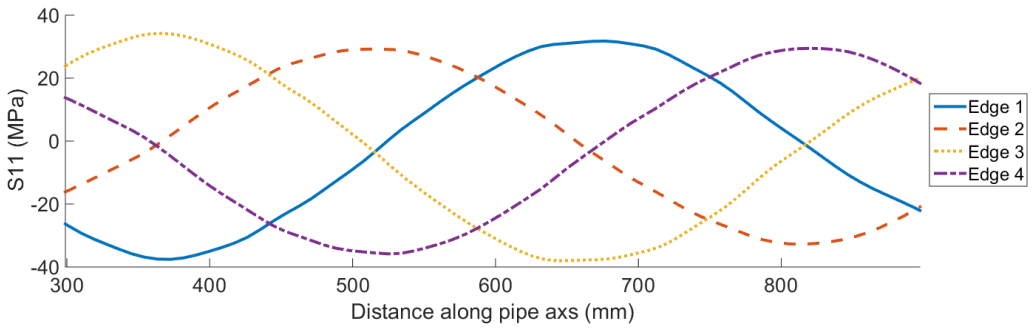

Figure 7-12: S11 along edges of wire-i-9 in model 3.

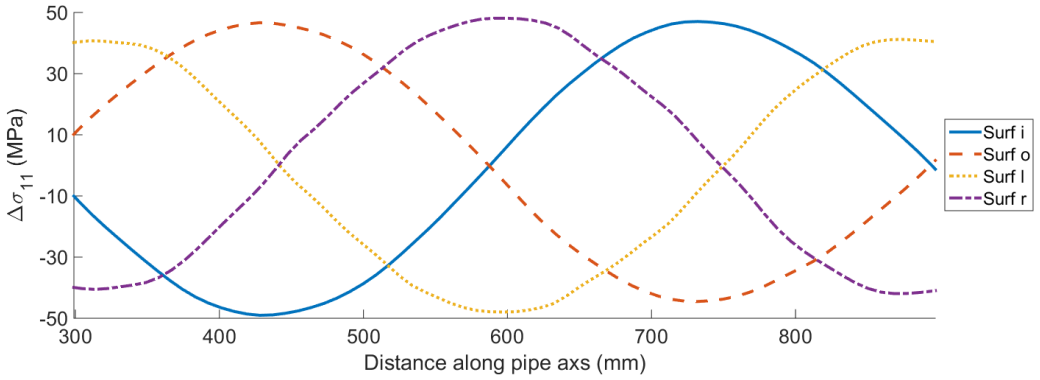

Figure 7-11: $\Delta\sigma_{11}$ along surfaces of wire-i-9 in model 3.

Table 7-6: Dynamic stress peaks in wire-i-9 in model 3.

	$\Delta\sigma_{11}^{M2}$		$\Delta\sigma_{11}^{M3}$	
Position mm	Inner surf.	Outer surf.	Left surf.	Right surf.
300	-	-	40.3	-40.3
450	-47.6	45.0	-	-
600	-	-	-48.0	48.1
750	46.3	-43.7	-	-
900	-	-	40.4	-40.5

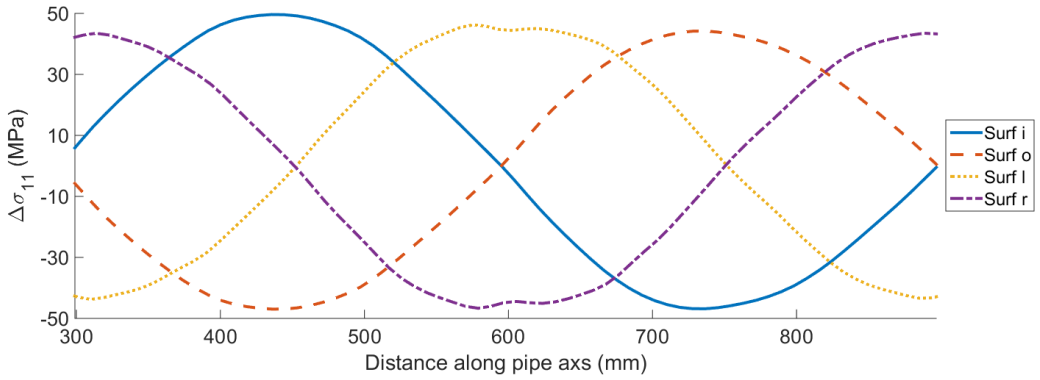

Figure 7-13: $\Delta\sigma_{11}$ along surfaces of wire-i-25 in model 3.

Table 7-7: Dynamic stress peaks in wire-i-25 in model 3.

	$\Delta\sigma_{11}^{M2}$		$\Delta\sigma_{11}^{M3}$	
Position mm	Inner surf.	Outer surf.	Left surf.	Right surf.
300	-	-	-43.0	42.9
450	49.2	-46.5	-	-
600	-	-	44.4	-44.4
750	-45.8	43.4	-	-
900	-	-	-42.2	42

The dynamic surface stresses ($\Delta\sigma_{11}$) for wire-o-10 and wire-o-28 are shown in **Figure 7-14** and **Figure 7-15**. The peak values are shown in **Table 7-8** and **Table 7-9**.

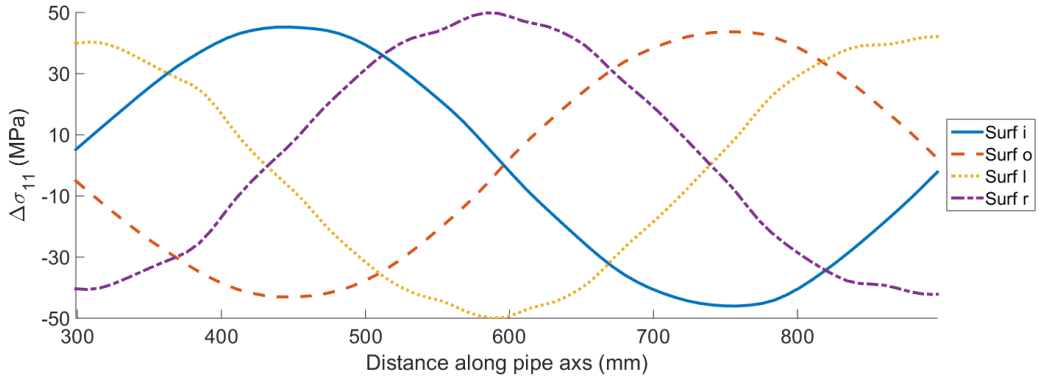

Figure 7-14: $\Delta\sigma_{11}$ along surfaces of wire-o-10 in model 3.

Table 7-8: Dynamic stress peaks in wire-o-10 in model 3.

	$\Delta\sigma_{11}^{M2}$		$\Delta\sigma_{11}^{M3}$	
Position mm	Inner surf.	Outer surf.	Left surf.	Right surf.
300	-	-	40.1	-40.3
450	45.3	-43.1	-	-
600	-	-	-48.6	48.6
750	-46	43.7	-	-
900	-	-	41.7	-41.9

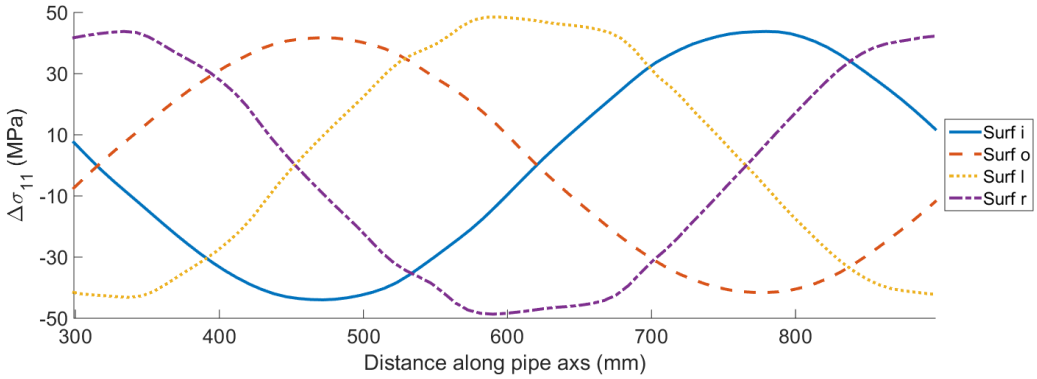

Figure 7-15: $\Delta\sigma_{11}$ along surfaces of wire-o-28 in model 3.

Table 7-9: Dynamic stress peaks in wire-o-28 in model 3.

	$\Delta\sigma_{11}^{M2}$		$\Delta\sigma_{11}^{M3}$	
Position mm	Inner surf.	Outer surf.	Left surf.	Right surf.
300	-	-	-42.0	41.8
450	-43	40.6	-	-
600	-	-	48.8	-48.4
750	43.0	-40.8	-	-
900	-	-	-42.3	42.3

As shown in **Figure 7-11** to **Figure 7-15**, the peak values of $\Delta\sigma_{11}^{M2}$ and $\Delta\sigma_{11}^{M3}$ occur at approximately the same locations as the analytical predictions. Dynamic stress ranges in all four wires are within the analytical limits. The stress due to normal curvature is closer to the geodesic assumption and the stress due to bi-normal curvature is about mid-range between the two limits. Similarly as for model 2, the stress along wire edges in model 3 is skewed towards the negative.

Comparing the surface stress results from model 2 and 3, one can see that the values are quite similar. However, stress peaks due to normal curvature are slightly larger for model 2. Furthermore, the plots of model 3 are slightly smoother than the ones of model 2. These differences could be due to the fact that solid and shell elements are based on different theories. Additionally, it is generally more difficult to model contact with shell elements, especially for multi-layered structures. This could result in increased contact stress on the inner and outer wire surface. All in all, both models are in agreement with the analytical predictions.

Looking at the deformation of the riser models in y-direction (U2) due to curvature of 0.06 radians, it is observed that the deformation mid-pipe in model 2 is about 0.0016% less than in model 3 (see **Figure 7-16**). For model 2, the radius and curvature is found to be 9.3646 m and 0.10678 m^{-1}. For model 3, the radius and curvature is found to be 9.3796 m and 0.10661 m^{-1}. The analytical radius and curvature is 10 m and 0.1 m^{-1}.

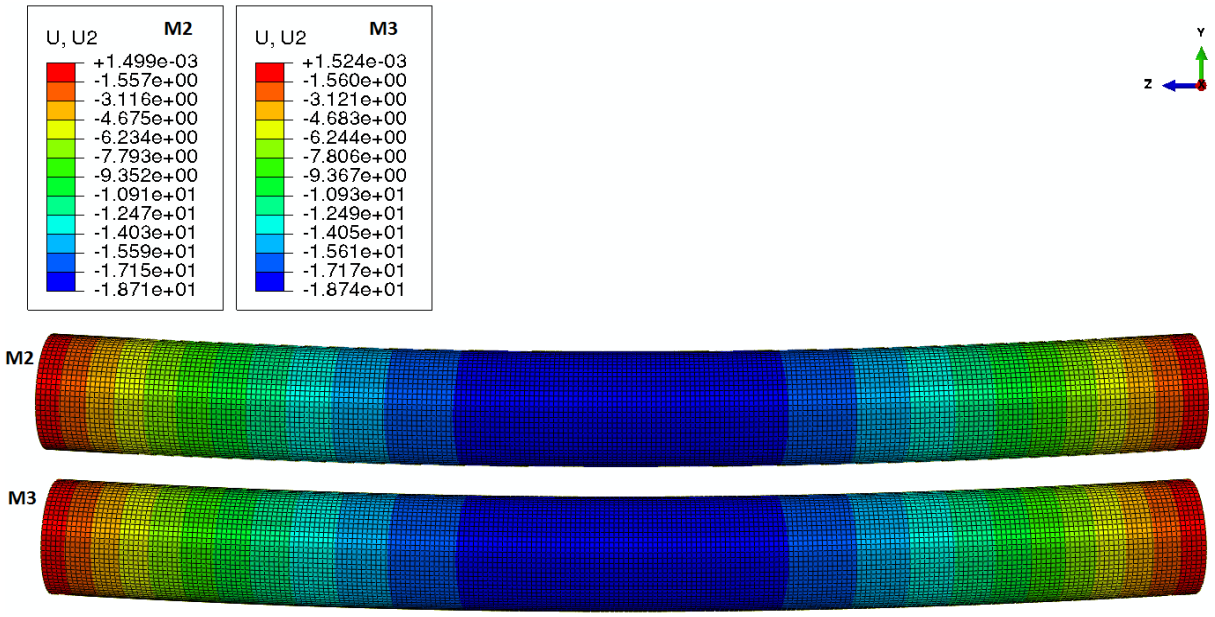

Figure 7-16: Model 2 and 3 deformation in y-direction (U2) due to curvature of 0.06 radians.

7.2 Damaged wires

Wire-o-27 and wire-o-28 in model 2 are modelled as broken in the damaged case. Approximately mid-pipe, the nine elements over wire cross section, numbered 622-630 are given four additional nodes each. The four original nodes and the duplicates have the same coordinates. After the additional nodes are introduced, elements 622-630 and the nine neighbouring elements are no longer connected. Thus, the two wires are free to separate between elements 622-630 and the neighbouring nine elements. The element numbering and convention used for node numbering are shown in **Figure 7-17**. Original nodes and duplicates in wire-o-27 and wire-o-28 are shown in **Table 7-10** and **Table 7-11**, respectively.

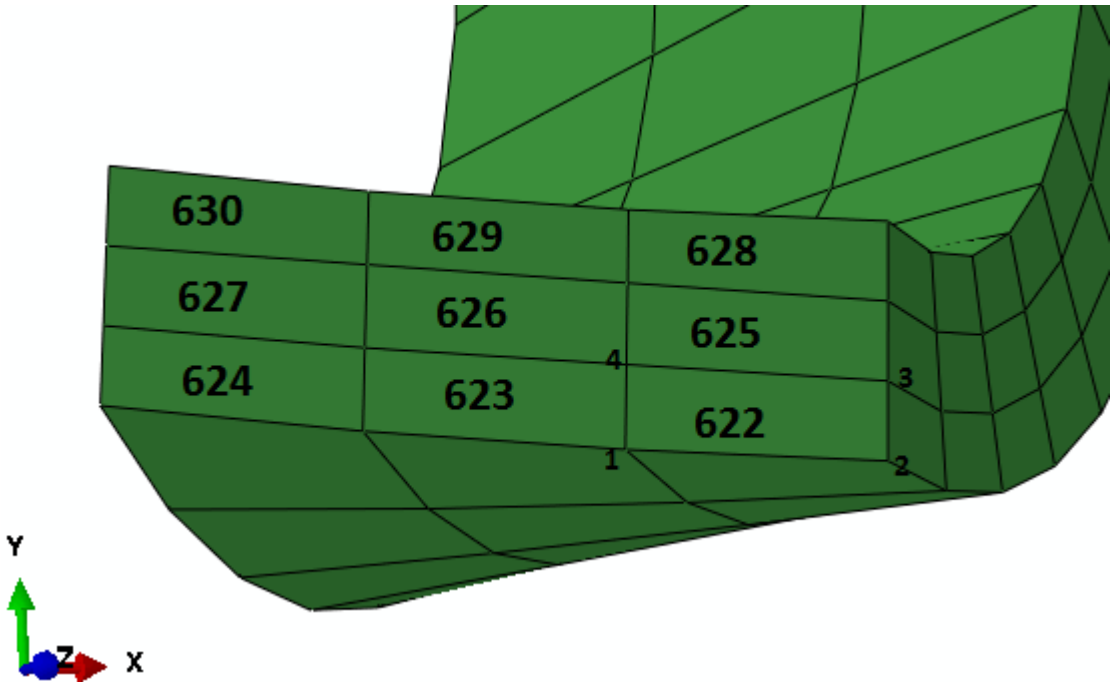

Figure 7-17: Numbered elements mid-pipe and convention for node numbering.

Table 7-10: Original and duplicate nodes in wire-o-27 simulating rupture.

node	1		2		3		4	
Element	Original	Duplic.	Original	Duplic.	Original	Duplic.	Original	Duplic.
622	1383	11383	395	10395	1215	11215	1977	11977
623	1384	11384	1383	11383	1977	11977	1978	11978
624	364	10364	1384	11384	1978	11978	1103	11103
625	1977	11977	1215	11215	1216	11216	1979	11979
626	1978	11978	1977	11977	1979	11979	1980	11980
627	1103	11103	1978	11978	1980	11980	1104	11104
628	1979	11979	1216	11216	305	10305	1047	11047
629	1980	11980	1979	11979	1047	11047	1048	11048
630	1104	11104	1980	11980	1048	11048	334	10334

Table 7-11: Original and duplicate nodes in wire-o-28 simulating rupture.

node	1		2		3		4	
Element	Original	Duplic.	Original	Duplic.	Original	Duplic.	Original	Duplic.
622	217	10217	15	10015	113	10113	1161	10161
623	218	10218	217	10217	1161	11161	1162	11162
624	13	10013	218	10218	1162	11162	95	10095
625	1161	11161	113	10113	112	10112	1163	11163
626	1162	11162	1161	11161	1163	11163	1164	11164
627	95	10095	1162	11162	1164	11164	96	10096
628	1163	11163	112	10112	10	10010	66	10066
629	1164	11164	1163	11163	66	10066	65	10065
630	96	10096	1164	11164	65	10065	9	10009

Tension

The damaged riser model is subject to the same tensile loading as the intact one. In the damaged case, however, axial stress is redistributed between the neighbouring intact wires and the largest stress concentration is found in wire-o-26 and wire-o-29 (see **Figure 7-18**). The mean axial wire stress ($S11_m$) is calculated for wire-o-26 in the intact and damaged riser by taking the average of S11 along the four wire edges. $S11_m$ is found to be about 245 MPa in the case of two ruptured wires which is about 19.1% more than in the intact case (see **Figure 7-19**). Stress concentration factors (SCF) in the current work are defined as the ratio between stresses in the intact and damage case. The mean axial wire stress ratio $\sigma_{11\text{-}Q1}{}^{d}/\ \sigma_{11\text{-}Q1}$ along wire-o-26 is shown in **Figure 7-20** and the average value is found to be 1.236 for the 2.5 inch considered in the current work. In the study by de Sosa [27], a FEA is performed for a flexible riser with one up to five broken wires in the outer layer. The riser is subject to pure tension and SCFs are calculated mid-pipe for the wires in the outer tensile layer. For two broken wires, the SCF for the intact wire closest to the broken ones is found to be 1.25, which is 1.1% higher than the result in the present work. The results are in good agreement, however, a 6 inch flexible riser is considered in de Sosa's study.

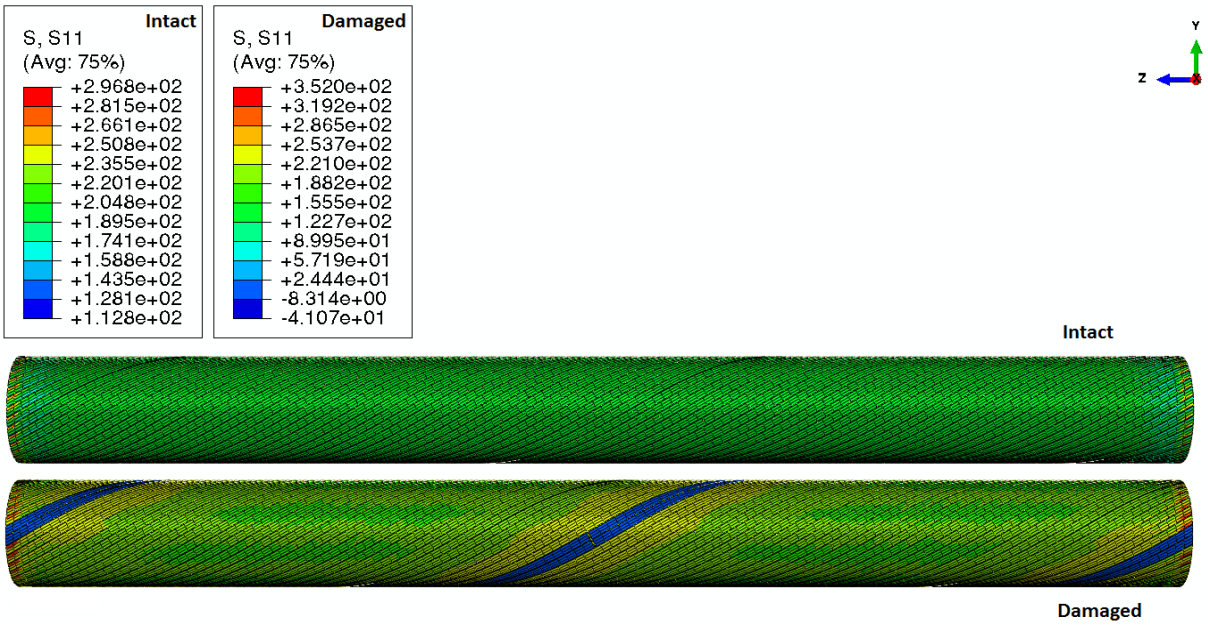

Figure 7-18: S11 in tensile wires in model 2 due to tension load of 250 kN for intact and damaged case.

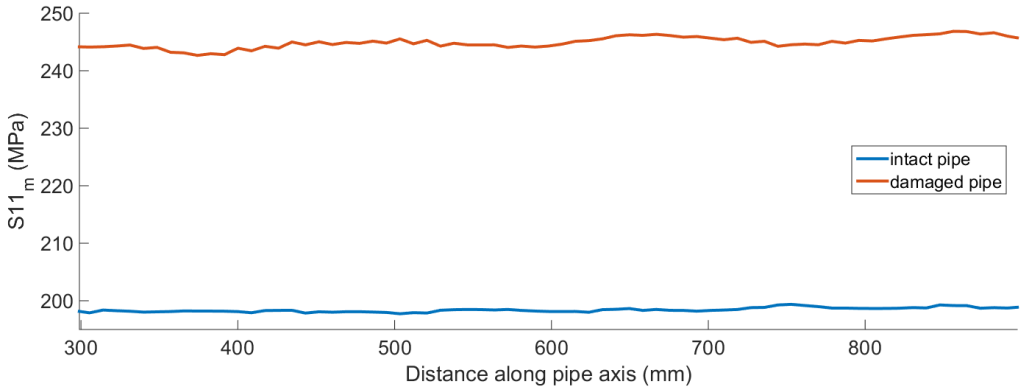

Figure 7-19: Mean axial wire stress ($S11_m$) in wire-o-26 of model 2 for the intact and damaged case.

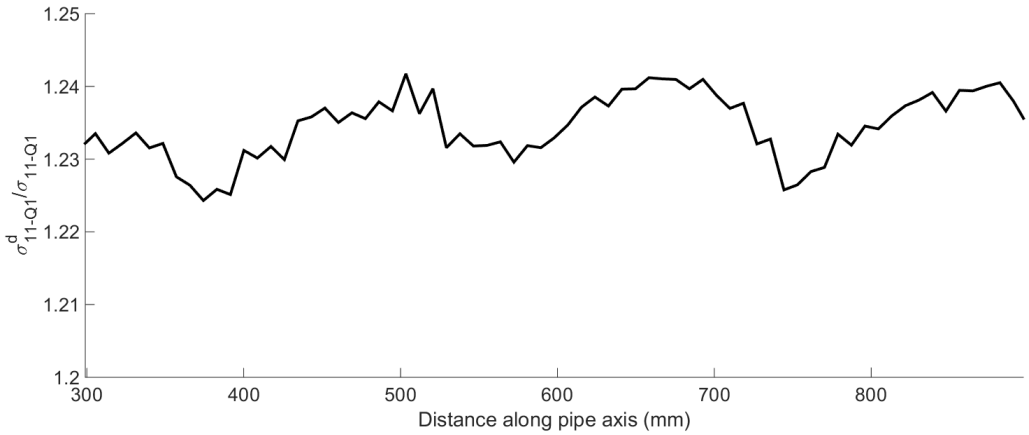

Figure 7-20: Mean axial wire stress ratio $\sigma_{11\text{-}Q1}{}^{d}/\ \sigma_{11\text{-}Q1}$ for wire-o-26 in model 2.

8 Conclusions and further recommendations

This work aimed at creating FE models suitable for integrity assessment of flexible riser with damaged tensile wires. Three models were developed to replicate a 2.5 inch flexible riser. Beam elements represented the tensile wires and shell elements the other layers in model 1. In model 2, solid elements represented the tensile wires and shell elements the other layers. Model 3 was modelled with solid elements in all layers. The carcass and pressure armour was modelled in a simplified manner with orthotropic material properties to reduce the computational effort of simulations.

A convergence study was performed in two parts to find the smallest number of elements needed to yield realistic results. The first part looked at global elements size and the second looked at number of elements over wire cross section. An axial load was applied at end 2 and the global displacement and axial wire stress was compared for different combinations of element sizes. It was found that the combination of global element size ten and nine elements over wire cross section yielded results close to the reference (global element size five and nine elements over wire cross section). The axial wire stress (S11) remained unchanged and the longitudinal displacement (U3) increased by only 0.004%.

The Equivalent material properties were evaluated by comparing hoop stress values (S22) to analytical calculations. An internal pressure was applied to the simplified carcass and pressure armour layer. S22 was measured mid-pipe at the internal wall. The results for carcass and pressure armour represented by shell elements was only 5% and 2% less than the analytical values, respectively. For solid elements, both results were 6.5% less than the analytical values. This deviation is acceptable considering analytical calculations are conservative in nature.

The axial stiffness of the riser models was investigated by simulating tensile loading. The axial load was applied at end 2 and the longitudinal deformation was divided by the riser length. The results was compared with the axial stiffness of the physical riser found in the literature. For model 2, the axial stiffness was found to be 3.4% larger than the physical riser. For model 3 it was only 0.001% less than the physical one.

Axial wire stress due to pipe bending was also investigated. The stress due to normal wire curvature ($\Delta\sigma_{11}^{M2}$) and bi-normal wire curvature ($\Delta\sigma_{11}^{M3}$) was calculated and compared to analytical values which assume wire paths during bending (geodesic and loxodromic). $\Delta\sigma_{11}^{M2}$ and $\Delta\sigma_{11}^{M3}$ for all wires considered in both model 2 and 3 were well within the analytical limits. Furthermore, the peak values occurred at the same positions along the riser as the analytical equations predicted.

Two wires in the outer tensile armour of model 2 was modelled as ruptured. Stress concentration factor (SCF) for the mean axial wire stress was calculated by dividing the stress in the neighbouring intact wire in the damaged case by the wire stress in the intact case. The SCF calculated in the current work was compared to results for a similar case found in the literature. The results were in good agreement as the SCF based on the present stress analysis was 1.1% less than the one found in the literature.

8.1 Recommendations for future work

The intact riser's response to pure tension and bending has been investigated in this thesis. However, the effects of more realistic load scenarios needs to be considered to justify the use of these models in integrity assessments. Load combinations like tension and bending with internal operational pressure should therefore be used in future analyses.

This work considered the riser with two ruptured wires in the outer layer and subject to tensile loading in the case of damaged tensile armour. Ruptured wires should be analysed in bending in addition to combined tension, bending and internal pressure to establish SCFs based on all components which contribute to the axial wire stress.

Model 1 presented in this work was not analysed. The tensile armours was modelled with beam elements which contain few nodes compared to the solid elements. Thus, model 1 could potentially be very efficient in stress analyses and should be investigated further.

This thesis has only laid a foundation which can be built on in future work on integrity assessment of flexible risers with damaged tensile armour. All mentioned above should be looked into for an increased number of ruptured wires. Torsional unbalance due to several ruptured wires might occur. The SCFs based on the combined load scenarios could be implemented in fatigue analysis to predict the remaining fatigue life of the riser.

Bibliography

[1] A. Luppi *et al.*, "Deepwater Hybrid Riser Systems," presented at the Offshore Technology Conf., Kuala Lumpur, Malaysia, 2014.

[2] "Un-bonded Flexible Risers – Recent Field Experience and Actions for Increased Robustness," 4Subsea, PSA-Norway, 2013.

[3] J. Muren, "Flexible Pipes, failure modes, inspection, testing and monitoring.," Seaflex, Norway, 2007.

[4] "Handbook on Design and Operation of Flexible Pipes," MARINTEK, 4Subsea, NTNU, Trondheim, 2014.

[5] S. Berge *et al.*, "Surface Characterisation and Fatigue Strength of Corroded Armour Wire," in *33rd Int. Ocean, Offshore and Artic Engineering Conf.*, San Francisco, Cal, 2014, p. V06BT04A015.

[6] G. Ji *et al.*, "Integrity Assessment of Damaged Flexible Pipe Cross-Sections," in *33rd Int. Ocean, Offshore and Artic Engineering Conf.*, San Francisco, Cal, 2014, p. V06BT04A020.

[7] J. R. M. de Sousa *et al.*, "A Methodology to Predict the Remaining Fatigue Life of a Flexible Pipe With Broken Tensile Armor Wires," in *Proc. 33rd Int. Ocean, Offshore and Artic Engineering Conf.*, San Francisco, Cal, 2014, p. V06AT04A061.

[8] J. A. Witz, "A case study in the cross-section analysis of flexible risers," *Marine Structures,* vol. 9, no. 9, pp. 885-904, 1996.

[9] A. B. Custódio and M. A. Vaz, "A nonlinear formulation for the axisymmetric response of umbilical cables and flexible pipes," *Applied Ocean Research,* vol. 24, pp. 21-29, 2002.

[10] J. R. M. de Sousa *et al.*, "On the Structural Response of a Flexible Pipe With Damaged Tensile Armor Wires," in *30th Int. Ocean, Offshore and Artic Engineering Conf.*, Rotterdam, The Netherlands, 2011, pp. 847-858.

[11] *Recommended practice for flexible pipe*, API RP 17B, 2008.

[12] *Specification for Unbonded Flexible Pipe*, API 17J, 2014.

[13] J. R. M. de Sousa *et al.*, "Bending Analysis of a Flexible Pipe With Broken Tensile Armor Wires," in *34th Int. Ocean, Offshore and Artic Engineering Conf.*, Newfoundland, Canada, 2015, p. V05AT04A038.

[14] S. Sævik, "Simplified models for predicting stress ranges due to dynamic bending," 2005.

[15] J. R. M. de Sousa *et al.*, "On the response of flexible risers to loads imposed by hydraulic collars," *Applied Ocean Research,* vol. 31, no. 3, pp. 157-170, 2009.

[16] W. Wang and G. Chen, "Analytical and numerical modeling for flexible pipes," *China Ocean Engineering,* journal article vol. 25, no. 4, pp. 737-746, 2011.

[17] S.-f. Ren *et al.*, "Behavior of unbonded flexible risers subject to axial tension," *China Ocean Engineering,* journal article vol. 28, no. 2, pp. 249-258, 2014.

[18] (2014). *ABAQUS 6.14 Documentation* [Online]. Available: http://50.16.225.63/v6.14/

[19] J. R. M. de Sousa *et al.*, "Numerical Analysis of a Flexible Pipe With Damaged Tensile Armor Wires," in *28th Int. Ocean, Offshore and Artic Engineering Conf.*, Honolulu, HI, 2009, pp. 829-839.

[20] S. Timoshenko and S. Woinowsky-Krieger, *Theory of plates and shells*, 2nd ed. New York: McGraw-Hill, 1959.

[21] M. J. Thorsen, "Capacity of Damaged Flexible Pipes," Unpublished.

[22] F. Irgens, *Fasthetslære*, 7th ed. Trondheim: Tapir akademisk forlag, 2006, p. 584.

[23] J. R. M. de Sousa *et al.*, "A Study on the Response of a Flexible Pipe to Combined Axisymmetric Loads," in *32nd Int. Ocean, Offshore and Artic Engineering Conf.*, Nantes, France, 2013, p. V04BT04A040.

[24] R. Walker. (2011). *Simetric [Online]*. Available: https://www.simetric.co.uk/si_metals.htm

[25] Matbase. *Engineering polymers [Online]*. Available: https://www.matbase.com/material-categories/natural-and-synthetic-polymers/thermoplastics/engineering-polymers/material-properties-of-polyamide-11-nylon-11-pa-11.html#properties

[26] A. C. Ugural and S. K. Fenster, *Advanced Strength and Applied Elasticity*. Elsevier, 1975.

[27] J. R. M. de Sousa *et al.*, "Fatigue Analysis of a 6" Flexible Pipe With Broken Tensile Armor Wires," in *32nd Int. Ocean, Offshore and Artic Engineering Conf.*, Rio de Janeiro. Brazil, 2012, no. 44908, pp. 445-457.